Efficient Plasmon-Mediated Energy Funneling to the Surface of Au@Pt Core–Shell Nanocrystals

Christian Engelbrekt,* Kevin T. Crampton, Dmitry A. Fishman, Matt Law, and Vartkess Ara Apkarian*

Cite This: *ACS Nano* 2020, 14, 5061–5074

Read Online

ACCESS | Metrics & More | Article Recommendations | SI Supporting Information

ABSTRACT: The structure and ultrafast photodynamics of ~8 nm Au@Pt core–shell nanocrystals with ultrathin (<3 atomic layers) Pt–Au alloy shells are investigated to show that they meet the design principles for efficient bimetallic plasmonic photocatalysis. Photoelectron spectra recorded at two different photon energies are used to determine the radial concentration profile of the Pt–Au shell and the electron density near the Fermi energy, which play a key role in plasmon damping and electronic and thermal conductivity. Transient absorption measurements track the flow of energy from the plasmonic core to the electronic manifold of the Pt shell and back to the lattice of the core in the form of heat. We show that strong coupling to the high density of Pt(d) electrons at the Fermi level leads to accelerated dephasing of the Au plasmon on the femtosecond time scale, electron–electron energy transfer from Au(sp) core electrons to Pt(d) shell electrons on the sub-picosecond time scale, and enhanced thermal resistance on the 50 ps time scale. Electron–electron scattering efficiently funnels hot carriers into the ultrathin catalytically active shell at the nanocrystal surface, making them available to drive chemical reactions before losing energy to the lattice via electron–phonon scattering on the 2 ps time scale. The combination of strong broadband light absorption, enhanced electromagnetic fields at the catalytic metal sites, and efficient delivery of hot carriers to the catalyst surface makes core–shell nanocrystals with plasmonic metal cores and ultrathin catalytic metal shells promising nanostructures for the realization of high-efficiency plasmonic catalysts.

KEYWORDS: core–shell nanocrystals, nanoparticles, Au@Pt, plasmonics, ultrafast carrier dynamics, photoelectron spectroscopy, photocatalysis
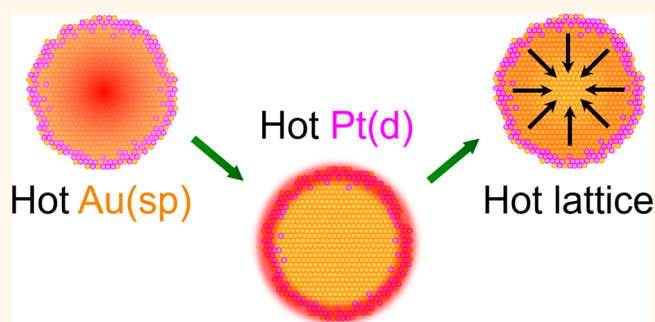
Plasmon-mediated catalysis has recently emerged as a promising new route for promoting chemistry initiated by the excitation of collective charge density oscillations in metal nanostructures.[1−6] At optical frequencies, coinage metals (Au, Ag, Cu) sustain bright localized surface plasmon resonances (LSPRs)[7] in which the net charge density is confined to within a few Å in the electron spill-out zone, at the interface where the dielectric function changes sign.[8,9] The large oscillator strength associated with these collective excitations enhances light–matter interactions through effects that are not found in conventional photocatalysts.[10−12] Due to their confinement, LSPs carry large local electric fields and their rapid dephasing and dissipation leads to excitation of interfacial states and generation of hot carriers, which in turn relax by releasing local heat. All of these phenomena can be exploited to increase reaction rates and product selectivity under relatively mild conditions compared to present catalysts.[13−16] Nanocrystals (NCs) of the coinage metals are

attractive because their LSPRs can be tuned across the visible-infrared spectrum by controlling NC size, shape and dielectric environment,[17,18] but their inherent chemical inertness limits their utility in catalysis. Bimetallic nanostructures that combine plasmonically active metals with catalytic transition metals (e.g., Pt, Pd, Rh, Ru) provide a logical route to efficient plasmon-driven catalysis,[3,19−29] be it in the form of antenna-reactor structures[22,23] or core–shell NCs.[3,19,27−37]

Here we investigate the structure and photodynamics of ~8 nm starch-capped Au@Pt core–shell NCs that possess

ACS Publications

atomically thin Pt−Au alloy shells. These NCs were previously demonstrated to be highly active (electro)catalysts for several organic transformations.[38,39] Their small size and ultrathin shell also make them promising nanostructures for efficient plasmon-driven catalysis. The small NC size is anticipated to promote efficient photocatalytic energy conversion by maximizing the quantum yield of light absorption and charge/energy transfer to molecules adsorbed on the catalytically active NC surface. Since optical extinction is dominated by absorption in small NCs and by scattering in large NCs,[40] small NCs avoid scattering losses and make efficient use of light for driving photocatalysis.[41] Mie calculations show that the ratio of scattering to absorption cross sections at the LSPR maximum of Au nanospheres in water increases from $<10^{-2}$ for NCs with a diameter $d < 25$ nm to >1 ($>50\%$ scattering losses) for $d > 90$ nm.[17,40,42,43] The negligible light scattering of small NCs should facilitate the design of high-efficiency plasmonic catalysts that do not require sophisticated light management. Moreover, small NCs ensure direct coupling of the Au LSP with molecules on the NC surface, promoting plasmon decay by ultrafast charge or energy transfer to adsorbates, often referred to as chemical interface damping or the "direct" mechanism of plasmonic catalysis.[11,24,44,45] Furthermore, all hot carriers generated in the core, both from the decay of the Au LSP and single electron intra/interband excitations, are produced within a fraction of an electron mean free path from the NC surface ($l_{mfp} \sim 40$ nm for Au at 298 K),[46,47] which facilitates their efficient transfer to adsorbed molecules (the "sequential" mechanism of plasmonic catalysis).[11,24,30,48,49] For these reasons, small core−shell NCs can provide particularly efficient photoabsorption and charge/energy delivery to surface catalytic sites. It is also worth noting that the maximum plasmonic electric field strength at the surface of an isolated Au NC depends only weakly on NC size,[41,50−52] while the average field enhancement integrated over the NC surface is larger for smaller NCs.[29] Intense local fields can trigger chemical reactions[53] and provide *in situ* probes of reaction mechanism via surface enhanced Raman spectroscopy (SERS).[54]

In addition to the size of the plasmonic NC, the thickness of the catalytic metal shell is also an important design parameter for optimizing the performance of core−shell NC photocatalysts. When the LSPRs of the core and shell are highly nondegenerate (due to the different free carrier density and effective mass in the two materials), shell electrons will make little contribution to the core LSP, and vice versa.[55,56] This is the case for our Au@Pt NCs (*vide infra*). In mechanical terms, the Au and Pt Fermi liquids have different viscosities, so the Pt electrons do not shake in resonance with the Au LSP. When the shell metal is nonplasmonic, ultrathin shells (1−3 atomic layers) will maximize the core plasmon field strength, plasmon−adsorbate coupling, and hot carrier density at the catalytic metal surface. Thicker shells only increase the distance and reduce the coupling between the plasmonic core and the NC surface, resulting in lower surface fields. Using SERS as the local field reporter, it has been experimentally demonstrated that one monolayer of Pt on an Au core leads to a dramatic ~90% drop in intensity,[57] an effect also recognized in other studies of bimetallic systems.[36,57−60] Besides fields, charge/energy transfer transitions will be weaker for thick shells due to the weaker plasmon-surface coupling, while hot carriers will lose energy as they move from the core through the shell to the NC surface. For example, approximately 20−30% of the hot carriers will scatter and lose some of their excess energy while transiting a 2 nm thick Pt shell (assuming $l_{mfp} = 5−10$ nm for Pt films).[61−64] The use of ultrathin shells minimizes these losses and takes best advantage of the localized field, charge, and energy density that an LSP provides. We note that potential drawbacks of ultrathin shells include lower stability in reaction conditions and more challenging characterization compared to NCs with thicker shells.

Bimetallic core−shell NCs are increasingly studied in the context of photocatalysis.[3,19,27−37] In 2013, Wang et al. reported the use of Au@Pd nanorods and NCs to perform Suzuki coupling reactions with low-intensity illumination.[19] The Majima group presented evidence for hot electron transfer from Au to Pt in photoexcited Au@Pt nanorods and triangular nanoprisms used to produce H_2 from water/methanol mixtures.[35,37] Huang et al. pointed out that nonplasmonic transition metal shells (*e.g.*, Pd, Pt) not only enhance molecular adsorption and reactivity, but also can increase the ratio of light absorption to scattering by virtue of their large imaginary dielectric permittivity (ε_2) at visible and near-infrared frequencies, which stems from their high density of d-states at the Fermi level and strong sp ← d interband transitions.[30] A combination of large ε_2 and high plasmonic field intensity ($|E|^2$) causes strong light absorption in the shell, effectively transferring light energy from the core to the surface of the NC. In cases where bulk dielectric functions can be used and interfacial quantum effects neglected (*e.g.*, for thick shells), the fraction of light absorption that occurs in the shell at each photon frequency ω can be written as $\frac{\int_{\text{shell}} \varepsilon_2(\omega, \mathbf{r})\, |\mathbf{E}(\omega, \mathbf{r})|^2\, d\mathbf{r}}{\int_{\text{core + shell}} \varepsilon_2(\omega, \mathbf{r})\, |\mathbf{E}(\omega, \mathbf{r})|^2\, d\mathbf{r}}$. Linic and co-workers used steady-state optical spectroscopy and classical electromagnetic simulations to show that shell absorption can dominate total light extinction in small Ag@Pt nanocubes and Au@Pt nanorods at frequencies where $\varepsilon_{2,\text{shell}} \gg \varepsilon_{2,\text{core}}$ and $|E|^2$ within the shell is large.[28,29] The resulting accumulation of energy at the NC surface (in the form of hot carriers and lattice heat) was used to increase the rate of CO oxidation.[28] Shell engineering creates many opportunities to direct the flow of electromagnetic energy to the surfaces of plasmonic NCs, but the dynamics of this energy funneling process are far from clear. Time-resolved measurements that map the flow of energy following LSP excitation can help guide the optimization of core−shell bimetallic nanostructures for energy-efficient photocatalysis.

In this paper, we utilize photoelectron spectroscopy (PES) to quantitatively determine the radial composition profile of our Au@Pt NCs as a function of Pt loading, 0−30 atom percent (at %), equivalent to 0−1.5 monolayers of Pt, and employ ultrafast transient absorption spectroscopy (TAS)[30,49,65] to track the NC photodynamics following LSP excitation. TAS has been used previously to study various photophysical processes in Au[66−71] and bimetallic NCs,[30,72−81] including electron−electron (e−e) and electron−phonon (e−p) scattering,[30,72−77] mechanical vibrations,[78−81] and thermal transfer to the environment. In particular, Hodak et al. found by single-wavelength TAS that Pt accelerates the decay of the LSPR bleach in Au@Pt and Pt@Au core−shell NCs.[73] The faster decay was attributed to faster carrier cooling in Pt, due to stronger e−p coupling. We show with global fits of TA spectra that the faster LSPR bleach is caused by rapid (<1 ps) e−e transfer from the Au core to the Pt shell that concentrates hot carriers in the catalytic surface layer of the NCs. We find that Pt dictates the energy flow on time scales from 10^{-15} to 10^{-10}
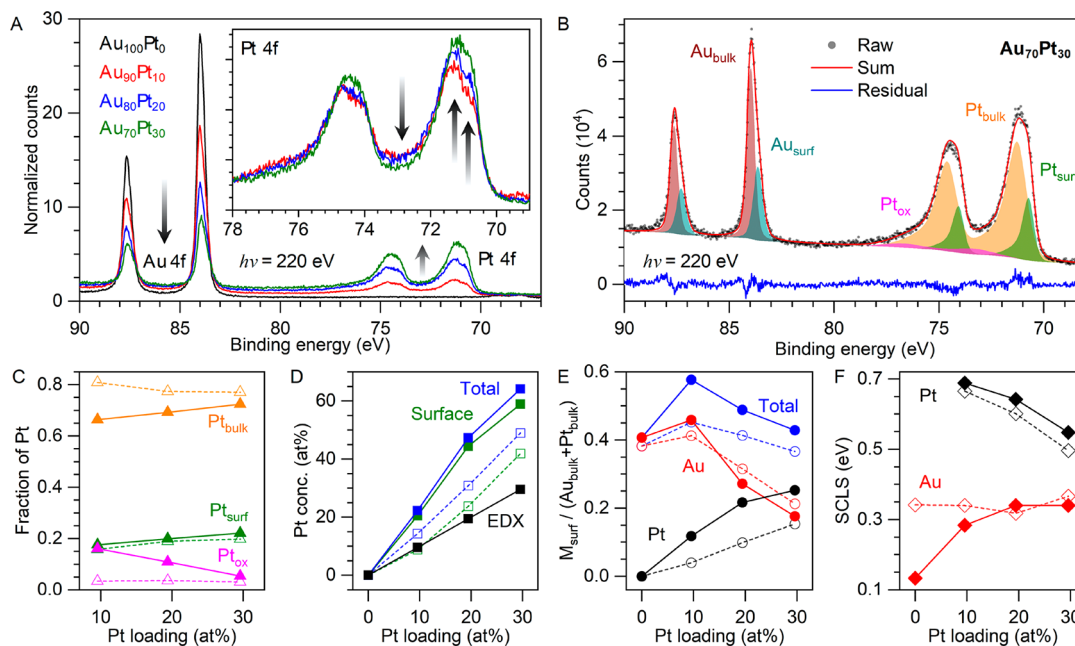
Figure 1. Chemical analysis of the Au and Au@Pt NCs with synchrotron PES. (A) High-resolution Au(4f) and Pt(4f) core-level spectra ($h\nu$ = 220 eV) normalized to the total area of the Au and Pt peaks to evaluate changes in NC composition with Pt loading. The inset shows a magnified view of the Pt(4f) spectra normalized to the total area of the Pt(4f) peaks to highlight the relative changes in the Pt components. Arrows indicate changes with increasing Pt loading. (B) An example of spectral deconvolution for the $Au_{70}Pt_{30}$ NC sample, where the Au(4f) peaks are fit with two symmetric spin−orbit doublets (splitting = 3.66 eV) to account for signals from bulk and surface Au atoms (Au_{bulk} and Au_{surf}), while the Pt(4f) peaks are fit with two asymmetric and one symmetric spin−orbit doublets (splitting = 3.34 eV) to account for signals from bulk, surface, and oxidized Pt atoms (Pt_{bulk}, Pt_{surf}, and Pt_{ox}). The figure shows the raw data (gray circles), contributions from each component (shaded areas), the sum of fit (red line), and the residual (blue line). Spectral deconvolutions for all samples are provided in Figure S5 and Table S1. The four bottom panels show (C) the fraction of Pt_{bulk}, Pt_{surf}, and Pt_{ox} as determined from the spectral fits, (D) the Pt/Au ratio of the surface components and total 4f signal compared to EDX data, (E) the ratio of surface components (Pt_{surf}, Au_{surf}, and Au_{surf} + Pt_{surf} in black, red, and blue, respectively) over the sum of bulk components (Au_{bulk} + Pt_{bulk}), and (F) the surface core level shifts (SCLSs), all as functions of Pt loading. In (C)−(F), solid lines and symbols denote data recorded at $h\nu$ = 220 eV, while dashed lines and open symbols denote data acquired at $h\nu$ = 700 eV.

s. On femtosecond time scales, the strong interfacial damping of the LSP and scattering on Pt(d) electrons is manifested by broadening of the Au LSPR. Notably, while strongly damped, the resonance frequency of the Au LSP and its integrated absorption cross section are preserved, illustrating that Pt(d) electrons do not participate in the collective charge density oscillations, as predicted in quantum treatments of Pt@Au core−shell NCs.[55] The Au core acts as the antenna for efficient light harvesting and the converted energy and charge density of the LSP is entirely dumped into the shell. The plasmon energy dissipates sequentially by e−e transfer from Au(sp) electrons in the core to Pt(d) electrons in the shell and subsequent "outside-in" heating of the lattice through e−p transfer from shell to core. On longer time scales, the higher thermal resistance of the Pt shell slows NC cooling with the surroundings. Our time-resolved measurements demonstrate that the electronic excitation of the Au core is dumped into the Pt shell on a sub-picosecond time scale, funneling light energy from the far field to the catalytic sites on the NC surface in the form of concentrated local fields, electronic heat (hot carriers) and lattice heat. Our results suggest that small bimetallic core−shell NCs with ultrathin shells are promising nanostructures for plasmon-driven chemical conversion.

RESULTS AND DISCUSSION

Synthesis of Au@Pt Nanocrystals. Starch-capped Au@Pt NCs were synthesized by reduction of $AuCl_4^-$ with MES buffer and subsequent reduction of $PtCl_6^{2-}$ by glucose (see Experimental Details).[38] The composition of the Au@Pt NCs was controlled by the amount of Pt added to the reaction (0, 10, 20, or 30 at % Pt on a metals basis). Energy dispersive X-ray (EDX) spectra of the purified sols showed that the added Pt is almost quantitatively incorporated into the NCs (89−97% incorporation, Figure S1), so we denote these four samples as $Au_{100}Pt_0$, $Au_{90}Pt_{10}$, $Au_{80}Pt_{20}$, and $Au_{70}Pt_{30}$ NCs. Analysis of transmission electron microscopy (TEM) images showed that the bare Au NCs are spheroids with a diameter of 7.3 ± 2 nm, increasing to 8.3 ± 2 nm for the $Au_{70}Pt_{30}$ NCs (Figures S2 and S3). TEM images also showed no evidence for pure Pt NCs in the samples, further confirming that the Pt preferentially deposits on the Au NC seeds to make bimetallic NCs, in agreement with previous results.[21]

It is useful to relate the measured Pt content to an idealized uniform Pt surface coverage ϑ:

$$\text{Pt at \%} = 100 \times \frac{V_s}{V_s + V_c} \frac{r_{Au}^3}{r_{Pt}^3} \tag{1}$$

where $V_c = 4\pi R_{core}^3/3$ is the Au NC core volume and $V_s \approx 8\pi\vartheta r_{Pt}(R_{core} + r_{Pt})^2$ is the volume of a monolayer Pt shell. For a core diameter $2R_{core}$ = 7.3 nm and metallic radii r_{Pt} = 1.38 Å and r_{Au} = 1.44 Å, the idealized Pt coverage of the four studied samples are ϑ = 0, 0.4, 0.9, and 1.5 monolayers of Pt. At the highest Pt loading, the NC diameter increases to $2R_{core} + 4\vartheta r_{Pt} \approx 8.13$ nm. Although consistent with TEM images, this

increase in diameter is smaller than the size dispersion of the NCs (Figure S3).

Structural Characterization by Photoelectron Spectroscopy. We have previously established the core−shell structure of our Au@Pt NCs using cyclic voltammetry and elemental mapping by high-resolution STEM-EDX spectroscopy.[38,39] Elemental maps acquired for the present work confirm the basic core−shell structure of the Au−Pt NCs (Figure S4). However, the limited spatial resolution of these maps does not allow quantification of the radial profile of the Pt concentration. Instead, we determine the radial profile of the Pt distribution from high-resolution photoelectron spectra recorded at incident photon energies of 220 and 700 eV, where both Au(4f) and Pt(4f) photoelectrons have effective attenuation lengths (EALs) of L = 0.43 and 0.87 nm, respectively.[82] Our chemical analysis, carried out through synchrotron PES of the four Au@Pt NC samples, is summarized in Figure 1. As expected, the 4f spectra in Figure 1A show a systematic increase in the Pt/Au atomic ratio as the Pt loading is increased. Five distinct spectral components are identified: two for Au and three for Pt. Th0.43 nm). Note that the Pt at % measured by PES metals exhibit bulk components at 84.00 ± 0.03 eV for Au and 71.32 ± 0.04 eV for Pt as well as undercoordinated (surface) components at 83.73 ± 0.09 eV for Au and 70.70 ± 0.03 eV for Pt. These assignments follow the established negative core level shift of undercoordinated surface atoms.[83,84] A representative spectral deconvolution is presented in Figure 1B, where a small contribution from oxidized Pt at 73.1 ± 0.3 eV is also identified. This is most prominent at the lowest Pt loading and is likely derived from organics, hydroxyl, or oxygen chemisorbed during NC synthesis.[84−87] The spectral decomposition quantitatively determines the Pt bulk, surface and oxidized contributions, which are shown in Figure 1C. Bulk Pt dominates at all Pt loadings, with a fairly constant fractionation between surface and bulk (S:B) of ∼1:3.5 (L = 0.43 nm). Note that the Pt at % measured by PES is significantly larger than the values obtained from EDX (Figure 1D). The latter interrogates the entire NC volume and reports the true overall composition, $[Pt]_{true}$. In contrast, PES interrogates the outer layers limited to a depth of ∼3L, yielding an apparent concentration, $[Pt]_{app}$, that is significantly higher than $[Pt]_{true}$. The enrichment factor EF = $[Pt]_{app}/[Pt]_{true}$ decreases from 2.2−2.4 at L = 0.43 nm ($h\nu$ = 220 eV) to 1.5−1.7 at L = 0.87 nm ($h\nu$ = 700 eV). This large difference in EF over a probe depth difference of only several atomic layers suggests a steep radial concentration gradient of Pt that is consistent with a Au@Pt core−shell NC structure.

The EF and S:B ratio measured at two energies (Figure 1C,D) is sufficient to reconstruct the radial distribution function of Pt. Treating the NCs as spheres, the apparent Pt fraction measured by PES is

$$[Pt]_{app} = \frac{\int_0^R n(s)\, P(s;L)(R-s)^2\, ds}{\int_0^R P(s;L)(R-s)^2\, ds} \quad (2)$$

in which R is the radius of the sphere, $s = R - r$ is the radial depth, $n(s)$ is the Pt radial density, and $P(s;L)$ is the photoemission probability, which in the shortest path escape limit takes the form of Beer's law: $P(s;L) = \exp(-s/L)$. The observable fractionation of Pt between surface and bulk:

$$Pt_{S:B} = \frac{\int_0^{\bar{r}} n(s)\, P(s;L)(R-s)^2\, ds}{\int_{\bar{r}}^R P(s;L)(R-s)^2\, ds} \quad (3)$$

is demarked by the choice of $\bar{r}$ as the mean atomic radius. Expressing $n(s)$ in a flexible Poissonian form:

$$n(s) = Nf(s) = Ns^\alpha\, e^{-\beta s} \quad (4)$$

with normalization (N) determined by the loading fraction:

$$[Pt]_{true} = \frac{\int_0^R n(s)(R-s)^2\, ds}{\int_0^R (R-s)^2\, ds} \quad (5)$$

The parameters α and β of the distribution function (eq 4) are overdetermined by the two measurements (eqs 2 and 3) at the two different photon energies for each true Pt distribution (eq 5). An iterative search leads to the distribution presented in Figure 2, in which Pt is seen to be limited to the outer two atomic layers.
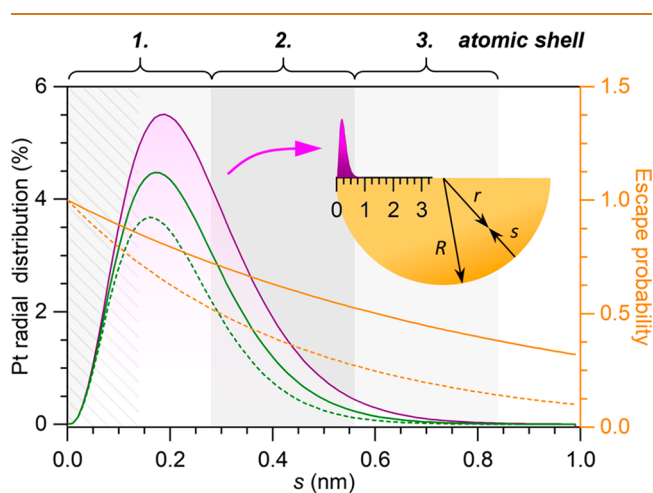
Figure 2. Radial concentration profile of Pt reconstructed from the PES data. (Purple trace) The true Pt distribution ($n(s)$ in eq 4) with parameters α = 2.8 and β = 15. (Green traces) The apparent Pt distributions ($n(s)P(s;L)$) for L = 0.87 nm (solid line)) and L = 0.43 nm (dashed line). (Orange traces, right axis) The corresponding escape probabilities ($P(s;L)$) that determine the interrogated volume. The distribution yields EF = $[Pt]_{app}/[Pt]_{true}$ = 2.2(1.7) and $Pt_{S/B}$ = 0.39(0.32) for L = 0.43(0.87) nm, in good agreement with the experimental values. The hashed area denotes the surface layer, and the three outer atomic layers are identified by the three tones of gray shading. The inset shows a model of a Au@Pt NC that defines the radial depth coordinate, s, in relation to the NC radius, R. The Pt distribution function (filled purple trace) is shown to scale.

The graph of the total S:B ratio in Figure 1E reveals surface roughening at 10% Pt loading (ϑ = 0.4). The increase in total S:B from 0.4 for bare Au to 0.6 implies a 50% increase in the number of surface atoms or a decrease of L, both of which may be rationalized by surface roughening (island formation). The roughening is accompanied by an increase in the Au S:B ratio, which implies displacement of Au atoms into the adlayer. The return of the total S:B ratio to ∼0.4 at 30% Pt loading (ϑ = 1.5) indicates smoothening of the surface. The crossing point of the Au and Pt S:B ratios, where the surface layer is composed of equal parts Au and Pt, occurs near 25% loading,

after addition of the equivalent of a monolayer of Pt atoms. This occurs as the surface roughening disappears, consistent with coalescence of the islands to form a smooth surface layer of a bimetallic Pt−Au alloy.

The above picture of the surface is consistent with prior studies of Pt deposition on Au substrates. At low coverage, Pt is known to form 2D islands on Au,[88] with Pt embedded in the surface and subsurface layer to form a bimetallic interface.[88−92] Scanning tunneling microscopy of Pt evaporated on Au(111) shows that Pt embeds in the surface layer at $\vartheta < 0.03$ and forms alloyed islands above this coverage with the Pt concentration of the islands increasing to 50% by the point of island coalescence.[91] Immiscibility and phase segregation in Au@Pt NCs have been observed by TEM, where, upon annealing, Pt segregates under a monolayer of Au,[93,94] consistent with theoretical predictions.[95,96]

The same picture is further supported by the observed core level shifts shown in Figure 1F. The evolution may be assigned to surface core level shifts (SCLSs) due to strain and ligand effects that change the electron binding energy of surface atoms,[89] and to charge transfer between Au and Pt due to the difference in their workfunctions.[92] The observed Pt SCLS is large (0.7 eV) at low coverage, when Pt atoms are located in an Au-rich environment. It continuously decreases to ∼0.55 eV as ϑ is increased and the surface alloy is enriched in Pt. The Au SCLS shows the opposite trend as the surface composition changes from Au-rich to Pt-rich.

Photoelectron spectra near the Fermi edge (E_F) probe the valence band density of states relevant to dynamics in optical excitations. Spectra recorded at $h\nu = 100$ eV are shown in Figure 3. In the bare Au NCs, E_F is located in the sp-band, 2.4
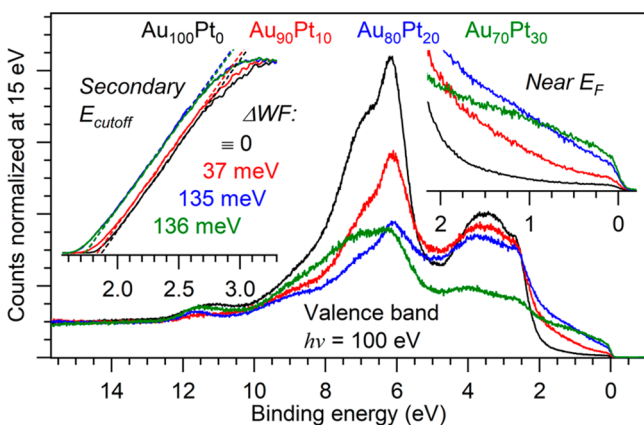

Figure 3. Valence band spectra of Au and Au@Pt NCs at $h\nu = 100$ eV. Right inset shows a magnification of the occupied states near E_F. Left inset shows the secondary electron cutoff energy and corresponding shifts in work function relative to pure Au NCs.

eV above the edge of the d-band marked by the sharp increase in the density of states (Figure 3, black trace). In contrast, E_F cuts through the d-band of Pt,[97] which is manifested by the increase in electron density between 0 and 2 eV with Pt loading (right inset in Figure 3). The decrease in the secondary electron cutoff energy (left inset in Figure 3) indicates a decrease in the surface work function with Pt loading. Although the work function of Pt is larger than that of Au, it is reduced at the Pt−Au interface to align with the Au Fermi level by withdrawing electron density from subsurface layers and forming an interfacial dipole.[50,92] This effect saturates at

$Au_{80}Pt_{20}$ ($\vartheta = 0.9$) as the islands coalesce into a smooth surface alloy.

Extinction Spectra and Femtosecond Dynamics. Normalized extinction spectra of the NCs recorded using a femtosecond white-light continuum are presented in Figure 4.
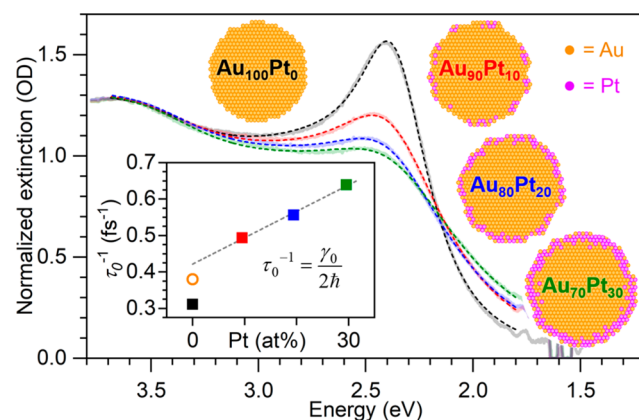
Figure 4. Extinction spectra and NC models. Normalized extinction spectra (solid lines) and fits (dashed lines) for $Au_{100}Pt_0$ (black), $Au_{90}Pt_{10}$ (red), $Au_{80}Pt_{20}$ (blue), and $Au_{70}Pt_{30}$ (green) NCs recorded using the TAS setup. The inset shows the plasmon dephasing rate (τ_0^{-1}) as a function of Pt content. The orange circle indicates the surface scattering rate (τ_s^{-1}) for an 8 nm Au NC with a scattering efficiency $\eta = 1$. Also shown are schematic representations of NC cross sections based on the PES analysis of the distributions of Au atoms (yellow) and Pt atoms (magenta) for each Pt loading. See Figure S6 for steady-state spectra normalized at the LSPR maxima.

At this NC size, the spectra are dominated by absorption,[42] which may be decomposed into three contributions:

$$A(E) = \overbrace{\frac{c_0}{\pi} \frac{\gamma_0/2}{(E-E_0)^2 + (\gamma_0/2)^2}}^{\text{LSP}} + \overbrace{\frac{c_1}{1 + e^{-\left(\frac{E-E_1}{\gamma_1}\right)}}}^{\text{vis IT}} + \overbrace{\frac{c_2}{1 + e^{-\left(\frac{E-E_2}{\gamma_2}\right)}}}^{\text{UV IT}}$$

(6)

consisting of a Lorentzian LSPR at $E_0 = 2.4$ eV with fwhm γ_0 and sp ← d interband transitions (ITs) mirroring the PES spectra (Figure 3), described by two switching functions at $E_1 = 2.4$ eV (vis IT) and $E_2 = 3.4$ eV (UV IT) with transition widths γ_1 and γ_2, respectively.[98]

The spectra may alternately be described through analytical models of the complex dielectric function fitted to experimental data.[98−102] However, such formulations are not well-defined for heterogeneous alloys. Here, the switching functions, which have the form $1 - f(E)$ where $f(E)$ is the Fermi function, describe the sp ← d interband transitions of Au, with widths determined by the dispersion $|d(E_{sp}-E_d)/dq|_{q_i}$ at the stationary points near $q_i = X$ and L for the UV and vis IT, respectively.[103−105] The spectra of the Au and Au@Pt NCs are reproduced using eq 6 with γ_0 and γ_1 as the only parameters that depend on Pt content (Figure 4, Table S2). Their perfectly correlated linear variation with loading (Figure S7) is manifested by an isosbestic point at 2.15 eV. Indeed, it has been previously noted that the spectra of Au@Pt NCs are characteristic of Au.[73,106]

Broadening of the Lorentzian riding over the vis IT leads to the apparent LSPR peak shift, while E_0 (the LSPR), which is determined by the electron density in the collective mode,

Table 1. Time Constants from the Spectral Domain (τ_0), Time-Dependent Fitting Parameters ($\tau_{\text{Au-Pt}}$, $\tau_{\text{e-p}}$), Long-Time Decay (τ_c), and Spectral Shifts a and b of Eq 9

sample	τ_0 [fs]^a	$\tau_{\text{Au-Pt}}$ [ps]	$\tau_{\text{e-p}}$ [ps]	τ_c [ps]	a [meV]	b [meV]
Au$_{100}$Pt$_0$	3.21 ± 0.01^b		1.9 ± 0.2^c	46 ± 1^b	20.4 ± 0.1^b	2.75 ± 0.06^b
Au$_{90}$Pt$_{10}$	2.03 ± 0.01^b	1.0 ± 0.2^c	2.2 ± 0.2^b	52 ± 2^b	3.8 ± 0.1^b	1.53 ± 0.04^b
Au$_{80}$Pt$_{20}$	1.80 ± 0.01^b	0.7 ± 0.2^c	2.1 ± 0.2^b	61 ± 2^b	11.5 ± 0.2^b	1.96 ± 0.04^b
Au$_{70}$Pt$_{30}$	1.57 ± 0.01^b	0.6 ± 0.2^c	2.3 ± 0.2^b	66 ± 1^b	9.5 ± 0.5^b	2.07 ± 0.05^b

^{a}The plasmon dephasing times τ_0 are obtained from the observed spectral widths, which include inhomogeneous broadening. The homogeneous dephasing times are 0.5−0.6 fs longer than the values of τ_0 (see text). ^{b}Standard error (SE) from fitting is reported as ± SE. ^{c}The averaged values are obtained as shown in Figure S11, and standard deviation (SD) from averaging is given as ± SD.

remains unchanged. Although the LSPR is incrementally broadened by the addition of Pt, its oscillator strength, determined by the number of participating electrons and measured by c_0, remains fairly constant: c_0 decreases by 6% at 30% Pt loading (see Table S2), and that decrease can be attributed to the charge transferred from Au to Pt at the core−shell interface. The constancy of E_0 and the oscillator strength of the LSPR are noteworthy: they establish that the LSP consists exclusively of the free Au(sp) electrons. Since the collective LSPR of Pt occurs near 215 nm,[107−109] its decoupling from the visible LSP of Au is not surprising. The electron−hole (e−h) pair excitations in the Pt shell, as with the e−p pairs created over the sp ← d interband transitions of the Au core, do not contribute to the collective charge density of the plasmon, which constitutes the screening response of free carriers to an external field.[8] It is worth noting that, in contrast to simple metals, screening by d-electrons in coinage metals plays an important role in determining the density profile of LSPs, and therefore the color and dispersion of their LSPR.[8,110,111] No such effect is evident by the Pt(d) manifold of the NC shell in the stationary extinction spectra (Figure 4).

The vis IT resonance at 2.4 eV is a reflection of the Au sp ← d transition seen in the PES of the Au NCs (black trace in Figure 3). The broadening of this interband transition with Pt loading is a direct indication of the extension of the Au electron wave functions (k-states) across the NCs, therefore their effective instantaneous scattering on the tightly bound Pt(d) electrons in the NC shell. The strength of the vis IT resonance, c_1, is otherwise unaffected by Pt loading. The featureless extinction continuum of Pt in the visible, which adds a sloping baseline,[38,106] is effectively removed by normalization of the spectra at 3.5 eV. The negligible contribution of the Pt extinction in the visible spectra renders the TAS data especially incisive, as we expand on below.

Information about the earliest time dynamics is obtained in the spectral domain. The Lorentzian width $\gamma_0 = 0.41$ eV of the Au NC LSPR, which implies a plasmon dephasing time of $\tau_0 = 2\hbar/\gamma_0 = 3.2$ fs,[112] agrees with prior measurements on 8 nm colloidal Au nanospheres.[69] The dephasing rate is assigned to the sum of bulk and surface contributions, τ_b and τ_s,[11] and a distinct contribution due to interfacial damping, τ_i[113]

$$\frac{1}{\tau_0} = \frac{1}{\tau_b} + \frac{1}{\tau_i} + \frac{1}{\tau_s} = \frac{1}{\tau_b} + \frac{1}{\tau_i} + \eta\frac{\nu_F}{R} \quad (7)$$

in which $\nu_F = 1.4 \times 10^6$ ms^{-1} is the Fermi velocity, R is the radius of the NC, and $\eta \leq 1$ is the surface scattering efficiency, determined by the structure and termination of the surface, which determine the potential that confines the plasmon.[114] Using $\tau_b = 5$ fs, obtained as the asymptotic limit of previous $1/R$-dependent measurements,[69] a value of $\eta = 0.3$ can be extracted for the Au NCs. The plot of the plasmon dephasing

rate, τ_0^{-1}, versus Pt loading (Figure 4, inset) shows a linear bulk contribution, with an intercept that exceeds the indicated limiting value of the surface scattering rate, ν_F/R (orange circle). The difference between the observed intercept and this limit is ascribed to interfacial damping, common to all Au@Pt NCs. It can be more simply interpreted as a contraction of the core radius due to the nonparticipation of Au atoms that transfer charge to Pt in the LSP. While surface roughening may accelerate plasmon damping,[11,48,115] the observed rate at 10% loading does not stand out as special. Note that plasmon dephasing by electron−hole pair creation occurs in an interfacial shell of thickness $\hbar\nu_F/E_0 \sim 4$ Å,[116] namely, the bimetallic layer at the surface of the NCs. Clearly, the collective Au plasmon mode dephases by scattering on the Pt(d) electrons, and the perfect correlation between γ_0 and γ_1 (Figure S7) implies that this holds for both collective and single particle excitation of Au(sp) electrons.

We should note that, given the size dispersion of the NCs, there must be an inhomogeneous contribution to the spectral widths. This can be estimated using the measured standard deviation in radii, $\sigma_R = \pm 0.85−0.95$ nm (Figure S2) in eq 7, to find that inhomogeneous broadening accounts for 0.5−0.6 fs, or 0.065−0.08 eV of the LSPR spectral width. The homogeneous plasmon dephasing times are therefore 0.5−0.6 fs longer than the uncorrected dephasing times τ_0 extracted from the spectral inversions and collected in Table 1 (e.g., 3.8 fs rather than 3.2 fs for the Au$_{100}$Pt$_0$ NCs).

Ultrafast Dynamics. The raw transient absorption spectra (Figure S8) are reduced by their parametric fit to eq 6 cast in standard form, $\Delta A(E,t) = A(E,t) - A(E,\infty) = \Delta A(\{\xi_t\})$, where $\{\xi_t\}$ is the time-dependent parameter set. We focus on the visible region, where the data can be adequately fit with $\{\xi_t\} = \{c_0, E_0, \gamma_0, c_1, \gamma_1\}_t$ representing the LSPR and vis IT. The adequacy of this treatment is illustrated in Figure 5, where we show a representative set of transient spectra (left) and their fits (right) for Au$_{100}$Pt$_0$ and Au$_{70}$Pt$_{30}$ NCs. Thus, the analysis of the governing ultrafast processes is reduced to interpreting the time profiles of physically motivated fitting parameters (collected in Figure S7).

Long-Time Lattice Cooling and Interfacial Thermal Resistance. The TA signal near the peak response at 2.5 eV (496 nm) is well determined at extended delay times (5 ps < t < 3 ns). On this time scale, the signal fits a biexponential decay (Figure S9). The first decay, with time constant $\tau_c \sim 50$ ps, is consistent with the previously reported cooling time of Au NCs in water,[117] while the second decay, with $\tau_{\text{solution}} > 500$ ps, is attributed to bulk heat diffusion from the irradiated volume to the rest of the solution. It has been suggested that a stretched exponential describes heat dissipation of Au NCs in this size range.[117] In our data, such a treatment yields similar rates but poorer fits (Figure S9). The systematic decrease in
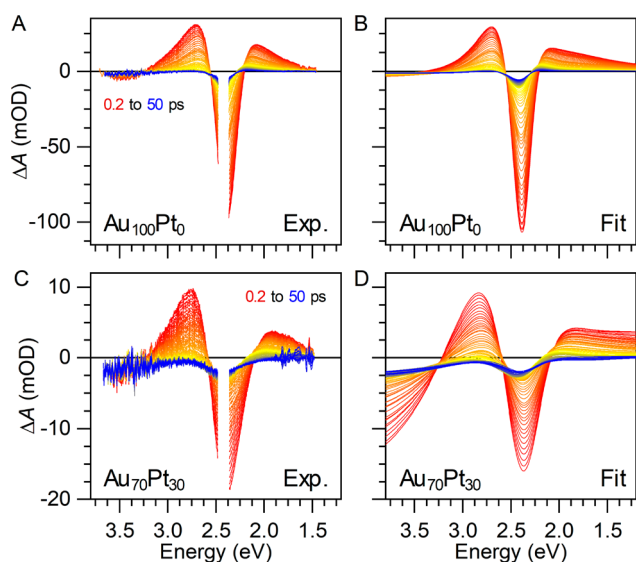
Figure 5. Transient absorption spectra. (A, C) Experimental TA spectra and (B, D) fitted spectra from 0.2 to 50 ps for $Au_{100}Pt_0$ and $Au_{70}Pt_{30}$ NCs. A narrow blind detection window at 512 nm is excluded due to signal contamination from pump pulse scattering.

the NC cooling rate with increased Pt loading is notable: τ_c increases from 46 ps for $Au_{100}Pt_0$ NCs to 66 ps for $Au_{70}Pt_{30}$ NCs (Figure 5C and Table 1). Even at the lowest loading ($\vartheta = 0.4$), Pt creates a bottleneck to heat flow. This is consistent with the thermal conductivity across interfaces between transition metals and coinage metals, where heat flow from the d-electron manifold to the sp-manifold is arrested.[118,119] The effect arises from the difference in electronic heat capacities, $C_e(T) = yT$, given by the Sommerfeld parameter, $y(T) = \pi^2 n_e(E_F) k_B^2 T/3$, determined by the electron density at the Fermi level, $n_e(E_F)$.[46] The 5:1 difference between d and sp electrons translates to a 5-fold smaller conductivity in Pt than in Au.[120,121] Dynamically, thermal conductivity is related to the electron–phonon (e–p) coupling parameter, $g(T)$, which is 40 times larger for Pt than Au at room temperature.[97] This contrast is more directly manifested at earlier time, during the equilibration of the electron and phonon reservoirs, which we consider next.

Early Time Electronic Cooling and Intermetallic e–e Scattering. With time resolution limited by the 0.1 ps pulse width of the laser, the early time dynamics that can be tracked during 0.1 ps < t < 5 ps is principally that of cooling of the thermalized Au(sp) electrons through e–p scattering, with concomitant heating and thermal expansion of the NC lattice.[74] The thermalization process is only evident in Au NCs, where $c_0(t)$ and $c_1(t)$ show a delay of ~400 fs, consistent with prior measurements.[122] Otherwise, common time constants determine the time profiles of all spectral fitting parameters (Figure S10 and Table 1).

The most incisive information is contained in the time profile of the LSPR energy, $E_0(t)$, which is presented in Figure 6A, along with the correlated time profile of its width, $\gamma_0(t)$, in Figure 6B. $E_0(t)$ tracks the plasmon frequency, $\omega_p = (n_e e^2/\varepsilon_0 m_e)^{1/2}$, determined by the free electron density, n_e.[46] It redshifts as n_e drops upon expansion of the heated electron gas, $\Delta E_{0,e} \propto -\Delta V_e \propto -\Delta T_e$, where V_e and T_e are the volume and temperature of the electron gas. Similarly, the LSPR redshifts as the lattice expands upon e–p energy transfer; therefore, $\Delta E_{0,L} \propto -\Delta V_L \propto -\Delta T_L$, where V_L and T_L are the volume and
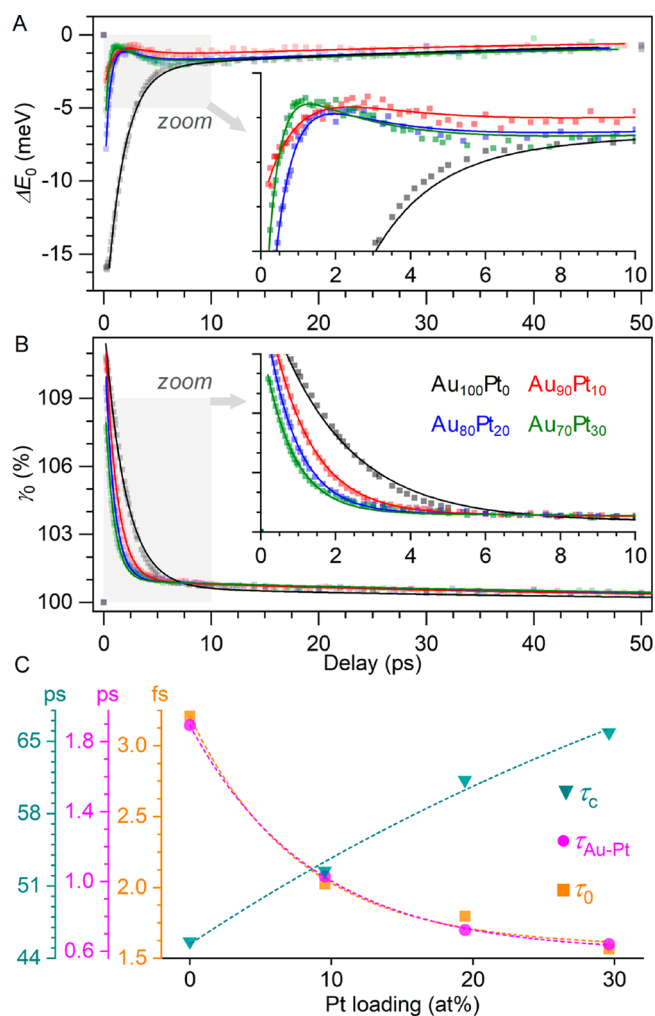
Figure 6. Time dependence of LSPR fitting parameters. Time traces of (A) E_0 and (B) γ_0 for $Au_{100}Pt_0$ (black), $Au_{90}Pt_{10}$ (red), $Au_{80}Pt_{20}$ (blue), and $Au_{70}Pt_{30}$ (green) NCs. Insets are magnified views of the first 10 ps (highlighted with the gray boxes). ΔE_0 in (A) is obtained by subtracting the steady state E_0 from all data points. Solid lines represent fits with the sequential kinetics expression in eq 11. (C) Pt loading dependence of the time constants for plasmon dephasing, τ_0 (orange squares), damping of Au(sp) electrons on the Pt(d) electrons, τ_{Au-Pt} (pink circles), and NC lattice cooling by coupling to the environment, τ_c (green triangles). Dotted lines represent exponential fits.

temperature of the atomic lattice. For $Au_{100}Pt_0$ NCs (no Pt), $\Delta E_0(t)$ fits a biexponential decay with time constants assigned as $\tau_{e-p} = 2$ ps and $\tau_c = 50$ ps (black trace in Figure 6A). The latter was assigned in the previous section to cooling of the lattice. The former is the thermal expansion time of the lattice, which limits the cooling rate of the thermalized electron gas. To be clear, τ_{e-p} represents the heat flow from electronic to lattice thermal reservoirs of distinct heat capacities, C_e and C_L, respectively:

$$T_e(Au) \underset{R_-}{\overset{R_+}{\rightleftarrows}} T_L(Au) \tag{8}$$

with forward rate $R_+ = g(T_e - T_L)/C_e$ and backward rate $R_- = g(T_e - T_L)/C_L$ formally given by the T-dependent e–p coupling, $g(T)$, and heat capacity, $C_e(T)$.[69] The observable spectral shift is therefore characterized by a single time constant:

$$\Delta E_0(t) = a' T_e(t) + b' T_L(t) = (a - b)\, e^{-t/\tau_{e-p}} + b \qquad (9)$$

in which a' and b' are proportionality constants that relate the temperatures to the observed LSPR shift, $a \equiv \Delta E_{0,e}$, $b \equiv \Delta E_{0,L}$, and $1/\tau_{e-p} = R_+ + R_-$ is rate limited by the adiabatic thermal expansion of the lattice.

The same 2 ps time constant appears in all ξ_t, a striking exception being the amplitude of the vis IT, $c_1(t)$, which shows a rise time of ~1 ps (Figure S10). Rise in the Au sp ← d absorption implies delay in filling of the optically generated Au(d) holes, which in turn implies transient e−p separation at the interface of the starch-capped Au NCs. The above picture abruptly changes upon Pt loading. It can be seen in Figure 6A that instead of the monotonic decay of $\Delta E_0(t)$ for the pure Au NCs, a sliding minimum develops at $t = 1-2$ ps for the different Pt loadings. The cooling of the Au electron reservoir is accelerated from 2 ps in $Au_{100}Pt_0$ to 0.6 ps in $Au_{70}Pt_{30}$ (τ_{Au-Pt}, see Table 1), separating it from the 2 ps thermal expansion time of the NC lattice, which now appears with an induction period characteristic of sequential kinetics:

$$T_e(Au) \rightarrow T_e(Pt) \rightleftharpoons T_L(Au) \qquad (10)$$

The sequence can be clearly seen in $\Delta E_0(t)$ because the LSPR shift singles out the Au electrons. $\Delta E_0(t)$ is given by the same weighted sum as in eq 9, reducing the observable LSPR shift for the sequential mechanism of eq 10 to

$$\Delta E_0(t) = a\, e^{-t/\tau_{Au-Pt}} + b\left[1 + \frac{\tau_{Au-Pt}\tau_{e-p}}{\tau_{Au-Pt} - \tau_{e-p}}\left(\frac{e^{-t/\tau_{e-p}}}{\tau_{Au-Pt}} - \frac{e^{-t/\tau_{Au-Pt}}}{\tau_{e-p}}\right)\right] \qquad (11)$$

in which τ_{Au-Pt} describes the damping of Au(sp) electrons through electron−electron scattering on Pt(d) electrons and τ_{e-p} describes equilibration of the Pt electronic reservoir with the phononic reservoir of the NC lattice. The fact that the same time constant, $\tau_{e-p} = 2$ ps, governs the direct (eq 8) and Pt-mediated (eq 10) heating (thermal expansion) of the lattice can be seen by the confluence of the time profiles of the LSPR shifts in Figure 6A.

The Au@Pt NC traces decompose the sum of the electron-cooling and lattice-heating processes, which as a sum of an exponential decay and rise of equal time constants generates the single decay profile in the bare Au NCs (a and b terms in eq 9). Treating it as a single exponential decay that measures τ_{e-p} would lead to assignment of the speed-up in Au@Pt NCs to acceleration of the e−p rate. This was done in the prior TAS study based on transients recorded at a single wavelength, which are otherwise nearly identical to the $\Delta E_0(t)$ data shown in Figure 6A (Figure 4 in ref 73). The rate-limiting step in equilibration of the electronic and phonon temperatures is the heating of the lattice, which proceeds on a time scale determined by the acoustic velocity. Indeed, the time constant τ_{e-p} common to all NCs can be estimated as $2R/v_{sound} = 2.3$ ps, where $v_{sound} = 3.2$ nm/ps is the speed of sound in gold and $2R = 7.3$ nm for the Au core. Note that sudden heating of Au NCs of this size should lead to breathing sphere oscillations with a period of 5 ps.[123] The absence of such oscillations may be attributed to the combination of surface roughness, which leads to capillary waves,[124,125] and dephasing due to the size dispersion of the NCs (inhomogeneous broadening).[74] The latter must be invoked in the case of the Au NCs, and therefore for the Au@Pt core−shell NCs as well.

We note that although they are on very different time scales, the dependence of τ_{Au-Pt} on Pt loading parallels that of the plasmon dephasing time, τ_0 (Figure 6C). As in the ultrafast dephasing of the plasmon, energy dissipation of the Au electrons occurs at the bimetallic shell on a time scale reaching $\tau_{Au-Pt} = 0.6$ ps in the $Au_{70}Pt_{30}$ NCs. Heating of the NC bulk must therefore proceed from outside-in (see illustration in Figure 7), driven by the electronic heat of the Pt(d) manifold.
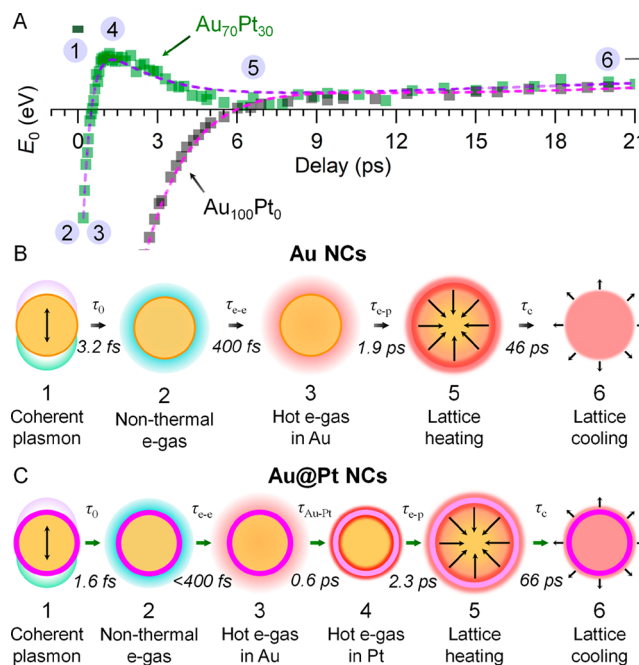
Figure 7. Main processes and their time scales following LSPR excitation of Au and Au@Pt NCs. (A) Time traces of the LSPR peak energy (E_0) for the $Au_{100}Pt_0$ NCs (black) and $Au_{70}Pt_{30}$ NCs (green), with the main processes numbered. **(B)** Schematic sequence and time constants (τ) for the $Au_{100}Pt_0$ NCs. (1 → 2) Plasmon damping followed by creation of a nonthermal electron gas. (2 → 3) Electron thermalization to form a hot carrier gas. (3 → 5) Lattice heating and expansion of the entire NC by electron−phonon equilibration. (5 → 6) NC cooling by heat transfer to the environment. **(C)** Schematic sequence and time constants (τ) for the $Au_{70}Pt_{30}$ NCs. (1 → 2) Plasmon damping. (2 → 3) Electron thermalization in the Au core. (3 → 4) Electron thermalization on Pt(d) electrons, energizing the Pt surface layer. (4 → 5) Outside-in lattice heating. (5 → 6) NC cooling.

It is useful to estimate the temperature of the thermalized electrons. For a simple Fermi liquid, the energy-dependent e−e scattering time is given as $\tau_{e-e}(E) = \tau[E_F/(E - E_F)]^2$, with experimentally determined $\tau = 5$ fs,[122] which is the same as τ_b extracted from the asymptotic limit of the plasmon dephasing time in eq 7. The slowing of relaxation times as $E \rightarrow E_F$ is due to the limitation of phase space, subject to the Pauli principle, which requires that both electrons remain above the Fermi level. This slowdown in e−e relaxation is where e−p equilibration takes over. Setting $\tau_{e-e}(E) = \tau_{e-p} = 2$ ps and taking $E_F = 5.5$ eV for gold,[46] yields $E - E_F = 0.275$ eV (~11 $k_B T$) as the available electron energy (temperature of the hot carriers) during the thermal expansion of the NCs. In the Au@Pt NCs, this energy is localized on electron−hole pairs created at Pt sites on the surface, priming their catalytic reactivity. Figure 7 summarizes the major processes following LSPR excitation of the Au and Au@Pt NCs.

The above picture is derived from the observed time constants. Also informative is the trend of the LSPR shift amplitudes (a and b) collected in Table 1. Both amplitudes show a dramatic drop at 10% Pt loading and then plateau at a significantly lower value than that of the bare Au NCs. The LSPR shift due to the lattice expansion, $b \equiv \Delta E_{0,L}$, may be used to extract the temperature rise of the lattice, ΔT_L:

$$\frac{\Delta E_{0,L}}{E_0} = \frac{\Delta V}{V} = \alpha_V \Delta T_L \tag{12}$$

in which $\alpha_V = 42 \times 10^{-6}$ K^{-1} is the volumetric thermal expansion coefficient of gold. The temperature rises by 32 K in the bare gold NCs, dips down to $\Delta T_L = 15$ K in the Au$_{90}$Pt$_{10}$ NCs and plateaus near $\Delta T_L = 20$ K as the shell coverage is completed (20−30 at % Pt). As a measure of the net energy density deposited in the NCs, the temperature rise should scale as $\Delta T_L \propto \sigma_a/V$, where σ_a is the absorption coefficient at the excitation wavelength (512 nm) and V is the volume of the NC. Using ΔT_L of the bare Au NCs as a reference, $\Delta T_L = 19$ K is predicted for the Au$_{70}$Pt$_{30}$ NCs, in good agreement with the experiment. However, the scaling predicts a monotonic decrease in ΔT_L due to the broadening of the LSPR with increasing Pt coverage and a plateau in the limit where the absorption cross section of the Pt shell scales by its volume. This scaling cannot explain the small ΔT_L at 10% Pt loading, which is nearly 50% smaller than the expected scaled value ($\Delta T_L = 27.7$ K). We recall that the LSPR shift measures the expansion of the Au core due to heat transfer from shell to core. The deficit found only for the case of the Au$_{90}$Pt$_{10}$ NCs must be associated with the roughening of the surface layer, which was established by the PES analysis (Figure 1). We speculate that energy trapped in lateral momentum of the shell (capillary waves) may not couple to the core on the 2 ps time scale. This is in part supported by the thermal bottleneck observed on the 50 ps time scale of cooling.

With regard to catalysis and energy transfer to the shell, more telling is the LSPR shift amplitude due to the Au electronic temperature, $a \equiv \Delta E_{0,e}$. Not surprisingly, the trend with Pt loading parallels that of $b \equiv \Delta E_{0,L}$ (see Table 1), but here the shift measures the thermalized density of e−p pairs in the core, long after the damping of the plasmon. In the case of the bare Au NCs, all e−p pairs that are created through Landau damping on the surface or in the bulk remain visible in our TA data. In the core−shell NCs, only the e−p pairs that remain in the core during the e−p relaxation time are observed in the TA spectra. As such, the dramatic ∼5-fold decrease in $\Delta E_{0,e}$ upon 10% Pt loading implies that ∼80% of electronic energy is in the shell and ∼20% in the core at 100 fs after photoexcitation. In the core−shell NCs with complete Pt coverage, this partitioning changes to ∼67% in the shell versus ∼33% in the core, presumably due to a different equilibration of carriers between shell and core. Although our TA data lack the time resolution needed to measure the branching ratio of plasmon decay into Pt e−p pairs versus Au e−p pairs, our results show that the fraction of energy present in the shell after short times (∼100 fs) is large (up to 0.8) and depends in a nontrivial way on the Pt coverage. Further study is needed to better understand and control the branching ratio of plasmon decay and subsequent energy flow for the direct and sequential mechanisms of plasmonic catalysis.

CONCLUSION

We utilized photoelectron spectroscopy and ultrafast transient absorption spectroscopy to characterize the structure and photophysics of ∼8 nm starch-capped Au@Pt core−shell NCs. PES carried out at two different photon energies shows that the NCs consist of Au cores covered by ultrathin (<3 atomic layers) bimetallic Pt−Au shells. The shell morphology evolves from islands at low Pt loading (10 at %) to a smooth continuous alloy layer at high Pt loading (30 at %). Pt addition progressively broadens the Au LSPR. This broadening is proof of strong electronic coupling between the Au LSP and the catalytic metal at the NC surface. At the same time, the resonance retains its integrated intensity to within 90% of the bare Au NC value, indicating that the number density and total number of electrons participating in the collective oscillations remain unchanged: the LSP belongs to the Au core of the core−shell NCs. While the reduced LSPR quality factor may lower absorption of monochromatic light, it is the integrated intensity that matters for broadband excitation such as sunlight. We calculate that the Pt-induced LSPR damping reduces total photon absorption by less than 10% for standard AM1.5G sunlight. Therefore, the Au@Pt NCs remain efficient absorbers of sunlight, which is a prerequisite for many applications in photocatalysis.

This study establishes that small Au@Pt NCs meet the photodynamic design principles of an efficient core−shell bimetallic plasmonic catalyst by maximizing the absorption quantum yield, plasmon-adsorbate coupling, and plasmonic field strength and hot carrier density at the catalytic surface sites. Our ultrafast transient absorption data show that up to 80% of the photon energy is contained in the ultrathin Pt shell at 100 fs after photoexcitation. The electronic excitation of the Au core is then entirely dumped into the Pt shell on a sub-picosecond time scale, funneling the hot carriers to the NC surface to drive chemistry. The electric field associated with the plasmon of the core, the hot carrier density it creates upon electron−electron scattering, and the hot carriers ($\Delta E = 0.275$ eV) that last for the 2 ps duration of electron−phonon relaxation are accessible to the ultrathin Pt−Au shell. An important design recommendation from this work is to use the thinnest catalytic shell necessary to achieve the desired chemical reactivity and structural stability, since thicker shells will only reduce plasmon−adsorbate coupling and lower the density and energy of hot carriers reaching the NC surface. Core−shell NCs with plasmonic cores and ultrathin catalytic shells are promising nanostructures for the future development of highly efficient plasmon-driven photocatalysts.

EXPERIMENTAL DETAILS

Materials. Tetrachloroauric acid trihydrate (HAuCl$_4$·3H$_2$O, Aldrich, ≥99.9%), hydrogen hexachloroplatinate(IV) hydrate (H$_2$PtCl$_6$·xH$_2$O, ≥99.9%, Aldrich), 2-(N-morpholino)ethanesulfonic acid (MES, ≥99.5%, Sigma), D-(+)-glucose (≥99.5%, Sigma), Zulkowsky starch (Sigma), potassium hydroxide (KOH, 99.99%, Sigma-Aldrich), and 2-propanol (IPA, HPLC grade, Fisher) were used as received. Ultrapure water (18.2 MΩ cm) was obtained from a Millipore Milli-Q system. A 0.1 M aqueous MES stock solution was made and adjusted to pH 8.0 with KOH.

Synthesis of Au@Pt Core−Shell Nanocrystals. The synthesis of Au@Pt NCs with varying Pt content was based on a modification of our published method.[38] First, colloidal Au NCs with a diameter of 7.3 ± 2 nm were synthesized by mixing 5 mL of 100 mM MES, 5 mL of 100 mM glucose, 15 mL of 2.0 wt % starch, and 20 mL of water in a round-bottom flask, heating the mixture to 95 °C, and rapidly

injecting 5 mL of 20 mM HAuCl$_4$. The temperature was maintained at 95 °C for 1 h before cooling to room temperature. Pt shells were grown by diluting 5.0 mL of the dark red Au NC dispersion with 14.78−14.94 mL of ultrapure water, adding either 60, 130, or 220 μL of 20 mM H$_2$PtCl$_6$ (20 mL total volume), and heating the mixture to 95 °C for 1 h to produce core−shell NCs with Pt molar loadings of 10, 20, and 30 at %, referred to here as Au$_{90}$Pt$_{10}$, Au$_{80}$Pt$_{20}$, and Au$_{70}$Pt$_{30}$ NCs, respectively. For transient absorption experiments, the as-synthesized Au@Pt NC sols were purified by flocculating with IPA (NC sol to IPA ratio of 1:5), centrifuging (3k RCF) and redispersing the NCs in ultrapure water. For X-ray photoelectron spectroscopy experiments, the as-synthesized Au@Pt NC sols were purified by centrifuging at 17k RCF, discarding the supernatant, and redispersing the sediment in ultrapure water.

Steady-State Optical Characterization. Steady-state optical extinction spectra were recorded on a PerkinElmer Lambda 950 spectrophotometer in 1 cm quartz cuvettes.

Transmission Electron Microscopy. Transmission electron microscopy (TEM) of the purified Au@Pt NCs was performed on a JEOL JEM-2800 transmission electron microscope equipped with a 4k × 4k Gatan OneView camera and dual 100 mm^2 silicon drift detectors for energy dispersive X-ray (EDX) spectroscopy. A volume of 5 μL of purified sample was drop cast on a TEM grid (01824G, Ted Pella) and dried in air. TEM data were processed using Gatan Digital Micrograph, Thermo NSS, and ImageJ software.[126]

X-ray Photoelectron Spectroscopy. X-ray photoelectron spectra of Au(4f), Pt(4f), and valence band states were acquired at the ANTARES beamline of Synchrotron SOLEIL (France) at photon energies of 100−700 eV. The purified sols were concentrated by centrifugation (17k RCF, 20 min) and drop cast (20 μL) onto Si substrates that had been sonicated in acetone, water, IPA, and water again, then subjected to UV-ozone treatment for 20 min (ProCleaner, Bioforce Nanosciences). The beamline was equipped with a Scienta R4000 hemispherical electron analyzer with a detection system based on a 40 mm diameter multichannel plate (MCP). The energy resolution was estimated by the full width at half-maximum (fwhm) of the first derivative of the Fermi edge to be 0.7 ± 0.1, 0.20 ± 0.04, and 0.13 ± 0.02 eV at photon energies of 700, 220, and 100 eV, respectively. Core level peak fitting was done with XPSPEAK41. Symmetric peak shapes were used for the Au(4f) peaks, while the Pt(4f) peaks were fit with an asymmetric peak shape (asymmetric function in XPSPEAK41).[89,127,128] The effective attenuation length (EAL) of photoelectrons was calculated using the NIST Electron Effective-Attenuation-Length Database ver. 1.3.

Ultrafast Transient Absorption Spectroscopy. Ultrafast transient absorption spectroscopy was performed using a chirped-pulse amplified Ti:Sapphire laser (Spitfire Ace, Spectra Physics, >7 mJ/pulse at 800 nm, 1 kHz) and an optical parametric amplifier (TOPAS Prime, Light Conversion) delivering 512 nm pump pulses (80 fs, 350 μJ/pulse/cm^2 on the sample) and supercontinuum white light probe pulses generated in a 2 mm CaF$_2$ crystal (325−900 nm). Transient absorption spectra of purified NC dispersions diluted with water to an optical density of 1.0 ± 0.3 at 512 nm were measured in 2 mm quartz cuvettes over the range of −10 ps to 3 ns with a fiber-coupled monochromator (MS260i, Newport) and CCD camera (LineSpec).

ASSOCIATED CONTENT

Ⓢ Supporting Information

The Supporting Information is available free of charge at https://pubs.acs.org/doi/10.1021/acsnano.0c01653.

> Experimental results including TEM, STEM-EDX, PES, UV−vis spectra, TA raw data and fitting (PDF)

AUTHOR INFORMATION

Corresponding Authors

Christian Engelbrekt − *Department of Chemistry, University of California Irvine, Irvine, California 92697, United States;* *Department of Chemistry, Technical University of Denmark, Kongens Lyngby 2800, Denmark;* ⓘ orcid.org/0000-0003-3679-3666; Email: cheng@kemi.dtu.dk

Vartkess Ara Apkarian − *Department of Chemistry, University of California Irvine, Irvine, California 92697, United States;* ⓘ orcid.org/0000-0002-7648-5230; Email: aapkaria@uci.edu

Authors

Kevin T. Crampton − *Department of Chemistry, University of California Irvine, Irvine, California 92697, United States;* ⓘ orcid.org/0000-0002-1258-7895

Dmitry A. Fishman − *Department of Chemistry, University of California Irvine, Irvine, California 92697, United States*

Matt Law − *Department of Chemistry, University of California Irvine, Irvine, California 92697, United States;* ⓘ orcid.org/0000-0001-7645-9908

Complete contact information is available at:
https://pubs.acs.org/10.1021/acsnano.0c01653

Author Contributions

C.E. designed the study and carried out synthesis, optical absorption, TEM and PES measurements. K.T.C. assisted with data analysis. D.A.F. performed the TA experiments. V.A.A. developed the PES and carrier dynamics models and directed the study with M.L. All authors were involved with data analysis and contributed to the writing of the manuscript. All authors have given approval to the final version of the manuscript.

Notes

The authors declare no competing financial interest.

REFERENCES

(1) Linic, S.; Christopher, P.; Ingram, D. B. Plasmonic-Metal Nanostructures for Efficient Conversion of Solar to Chemical Energy. *Nat. Mater.* **2011**, *10*, 911−921.

(2) Hou, W.; Cronin, S. B. A Review of Surface Plasmon Resonance-Enhanced Photocatalysis. *Adv. Funct. Mater.* **2013**, *23*, 1612−1619.

(3) Sytwu, K.; Vadai, M.; Dionne, J. A. Bimetallic Nanostructures: Combining Plasmonic and Catalytic Metals for Photocatalysis. *Adv. Phys. X* **2019**, *4*, 1619480.

(4) Aslam, U.; Rao, V. G.; Chavez, S.; Linic, S. Catalytic Conversion of Solar to Chemical Energy on Plasmonic Metal Nanostructures. *Nat. Catal.* **2018**, *1*, 656−665.

(5) Brooks, J. L.; Warkentin, C. L.; Saha, D.; Keller, E. L.; Frontiera, R. R. Toward a Mechanistic Understanding of Plasmon-Mediated Photocatalysis. *Nanophotonics* **2018**, *7*, 1697−1724.

(6) Mubeen, S.; Lee, J.; Singh, N.; Krämer, S.; Stucky, G. D.; Moskovits, M. An Autonomous Photosynthetic Device in Which All

Charge Carriers Derive from Surface Plasmons. *Nat. Nanotechnol.* **2013**, *8*, 247−251.

(7) Ritchie, R. H. Plasma Losses by Fast Electrons in Thin Films. *Phys. Rev.* **1957**, *106*, 874−881.

(8) Liebsch, A. Dynamical Screening at Simple-Metal Surfaces. *Phys. Rev. B: Condens. Matter Mater. Phys.* **1987**, *36*, 7378−7388.

(9) Maier, S. A. *Plasmonics: Fundamentals and Applications*; Springer US: New York, 2007.

(10) Brongersma, M. L.; Halas, N. J.; Nordlander, P. Plasmon-Induced Hot Carrier Science and Technology. *Nat. Nanotechnol.* **2015**, *10*, 25−34.

(11) Hartland, G. V.; Besteiro, L. V.; Johns, P.; Govorov, A. O. What's So Hot About Electrons in Metal Nanoparticles? *ACS Energy Lett.* **2017**, *2*, 1641−1653.

(12) Besteiro, L. V.; Kong, X. T.; Wang, Z.; Hartland, G.; Govorov, A. O. Understanding Hot-Electron Generation and Plasmon Relaxation in Metal Nanocrystals: Quantum and Classical Mechanisms. *ACS Photonics* **2017**, *4*, 2759−2781.

(13) Cortés, E. Efficiency and Bond Selectivity in Plasmon-Induced Photochemistry. *Adv. Opt. Mater.* **2017**, *5*, 1700191.

(14) Quiroz, J.; Barbosa, E. C. M.; Araujo, T. P.; Fiorio, J. L.; Wang, Y. C.; Zou, Y. C.; Mou, T.; Alves, T. V.; De Oliveira, D. C.; Wang, B.; Haigh, S. J.; Rossi, L. M.; Camargo, P. H. C. Controlling Reaction Selectivity over Hybrid Plasmonic Nanocatalysts. *Nano Lett.* **2018**, *18*, 7289−7297.

(15) Marimuthu, A.; Zhang, J.; Linic, S. Tuning Selectivity in Propylene Epoxidation by Plasmon Mediated Photo-Switching of Cu Oxidation State. *Science* **2013**, *339*, 1590−1593.

(16) Avanesian, T.; Christopher, P. Adsorbate Specificity in Hot Electron Driven Photochemistry on Catalytic Metal Surfaces. *J. Phys. Chem. C* **2014**, *118*, 28017−28031.

(17) Amendola, V.; Pilot, R.; Frasconi, M.; Maragò, O. M.; Iatì, M. A. Surface Plasmon Resonance in Gold Nanoparticles: A Review. *J. Phys.: Condens. Matter* **2017**, *29*, 203002.

(18) Kelly, K. L.; Coronado, E.; Zhao, L. L.; Schatz, G. C. The Optical Properties of Metal Nanoparticles: The Influence of Size, Shape, and Dielectric Environment. *J. Phys. Chem. B* **2003**, *107*, 668−677.

(19) Wang, F.; Li, C.; Chen, H.; Jiang, R.; Sun, D.; Li, Q.; Wang, J.; Yu, J. C.; Yan, C. Plasmonic Harvesting of Light Energy for Suzuki Coupling Reactions. *J. Am. Chem. Soc.* **2013**, *135*, 5588−5601.

(20) Yonezawa, T.; Toshima, N. Polymer- and Micelle-Protected Gold/Platinum Bimetallic Systems. Preparation, Application to Catalysis for Visible-Light-Induced Hydrogen Evolution, and Analysis of Formation Process with Optical Methods. *J. Mol. Catal.* **1993**, *83*, 167−181.

(21) Wang, D.; Li, Y. Bimetallic Nanocrystals: Liquid-Phase Synthesis and Catalytic Applications. *Adv. Mater.* **2011**, *23*, 1044−1060.

(22) Swearer, D. F.; Zhao, H.; Zhou, L.; Zhang, C.; Robatjazi, H.; Martirez, J. M. P.; Krauter, C. M.; Yazdi, S.; McClain, M. J.; Ringe, E.; Carter, E. A.; Nordlander, P.; Halas, N. J. Heterometallic Antenna−Reactor Complexes for Photocatalysis. *Proc. Natl. Acad. Sci. U. S. A.* **2016**, *113*, 8916−8920.

(23) Robatjazi, H.; Zhao, H.; Swearer, D. F.; Hogan, N. J.; Zhou, L.; Alabastri, A.; McClain, M. J.; Nordlander, P.; Halas, N. J. Plasmon-Induced Selective Carbon Dioxide Conversion on Earth-Abundant Aluminum-Cuprous Oxide Antenna-Reactor Nanoparticles. *Nat. Commun.* **2017**, *8*, 27.

(24) Zhang, Y.; He, S.; Guo, W.; Hu, Y.; Huang, J.; Mulcahy, J. R.; Wei, W. D. Surface-Plasmon-Driven Hot Electron Photochemistry. *Chem. Rev.* **2018**, *118*, 2927−2954.

(25) Blaber, M. G.; Arnold, M. D.; Ford, M. J. A Review of the Optical Properties of Alloys and Intermetallics for Plasmonics. *J. Phys.: Condens. Matter* **2010**, *22*, 143201.

(26) Swearer, D. F.; Robatjazi, H.; Martirez, J. M. P.; Zhang, M.; Zhou, L.; Carter, E. A.; Nordlander, P.; Halas, N. J. Plasmonic Photocatalysis of Nitrous Oxide into N2 and O2 Using Aluminum−Iridium Antenna−Reactor Nanoparticles. *ACS Nano* **2019**, *13*, 8076−8086.

(27) Joplin, A.; Hosseini Jebeli, S. A.; Sung, E.; Diemler, N.; Straney, P. J.; Yorulmaz, M.; Chang, W. S.; Millstone, J. E.; Link, S. Correlated Absorption and Scattering Spectroscopy of Individual Platinum-Decorated Gold Nanorods Reveals Strong Excitation Enhancement in the Nonplasmonic Metal. *ACS Nano* **2017**, *11*, 12346−12357.

(28) Aslam, U.; Chavez, S.; Linic, S. Controlling Energy Flow in Multimetallic Nanostructures for Plasmonic Catalysis. *Nat. Nanotechnol.* **2017**, *12*, 1000−1005.

(29) Chavez, S.; Aslam, U.; Linic, S. Design Principles for Directing Energy and Energetic Charge Flow in Multicomponent Plasmonic Nanostructures. *ACS Energy Lett.* **2018**, *3*, 1590−1596.

(30) Huang, H.; Zhang, L.; Lv, Z.; Long, R.; Zhang, C.; Lin, Y.; Wei, K.; Wang, C.; Chen, L.; Li, Z.-Y.; Zhang, Q.; Luo, Y.; Xiong, Y. Unraveling Surface Plasmon Decay in Core−Shell Nanostructures toward Broadband Light-Driven Catalytic Organic Synthesis. *J. Am. Chem. Soc.* **2016**, *138*, 6822−6828.

(31) Zhu, X.; Jia, H.; Zhu, X. M.; Cheng, S.; Zhuo, X.; Qin, F.; Yang, Z.; Wang, J. Selective Pd Deposition on Au Nanobipyramids and Pd Site-Dependent Plasmonic Photocatalytic Activity. *Adv. Funct. Mater.* **2017**, *27*, 1700016.

(32) Ranno, L.; Forno, S. D.; Lischner, J. Computational Design of Bimetallic Core-Shell Nanoparticles for Hot-Carrier Photocatalysis. *npj Comput. Mater.* **2018**, *4*, 31.

(33) Zeng, J.; Zhu, C.; Tao, J.; Jin, M.; Zhang, H.; Li, Z. Y.; Zhu, Y.; Xia, Y. Controlling the Nucleation and Growth of Silver on Palladium Nanocubes by Manipulating the Reaction Kinetics. *Angew. Chem., Int. Ed.* **2012**, *51*, 2354−2358.

(34) Huang, X.; Li, Y.; Chen, Y.; Zhou, H.; Duan, X.; Huang, Y. Plasmonic and Catalytic AuPd Nanowheels for the Efficient Conversion of Light into Chemical Energy. *Angew. Chem., Int. Ed.* **2013**, *52*, 6063−6067.

(35) Zheng, Z.; Tachikawa, T.; Majima, T. Single-Particle Study of Pt-Modified Au Nanorods for Plasmon-Enhanced Hydrogen Generation in Visible to Near-Infrared Region. *J. Am. Chem. Soc.* **2014**, *136*, 6870−6873.

(36) Zhang, C.; Chen, B. Q.; Li, Z. Y.; Xia, Y.; Chen, Y. G. Surface Plasmon Resonance in Bimetallic Core-Shell Nanoparticles. *J. Phys. Chem. C* **2015**, *119*, 16836−16845.

(37) Lou, Z.; Fujitsuka, M.; Majima, T. Pt-Au Triangular Nanoprisms with Strong Dipole Plasmon Resonance for Hydrogen Generation Studied by Single-Particle Spectroscopy. *ACS Nano* **2016**, *10*, 6299−6305.

(38) Engelbrekt, C.; Šešelj, N.; Poreddy, R.; Riisager, A.; Ulstrup, J.; Zhang, J. Atomically Thin Pt Shells on Au Nanoparticle Cores: Facile Synthesis and Efficient Synergetic Catalysis. *J. Mater. Chem. A* **2016**, *4*, 3278−3286.

(39) Šešelj, N.; Engelbrekt, C.; Ding, Y.; Hjuler, H. A.; Ulstrup, J.; Zhang, J. Tailored Electron Transfer Pathways in Au$_{core}$/Pt$_{shell}$-Graphene Nanocatalysts for Fuel Cells. *Adv. Energy Mater.* **2018**, *8*, 1702609.

(40) Tcherniak, A.; Ha, J. W.; Dominguez-Medina, S.; Slaughter, L. S.; Link, S. Probing a Century Old Prediction One Plasmonic Particle at a Time. *Nano Lett.* **2010**, *10*, 1398−1404.

(41) Geonmonond, R. S.; da Silva, A. G. M.; Rodrigues, T. S.; de Freitas, I. C.; Ando, R. A.; Alves, T. V.; Camargo, P. H. C. Addressing the Effects of Size-Dependent Absorption, Scattering, and Near-Field Enhancements in Plasmonic Catalysis. *ChemCatChem* **2018**, *10*, 3447−3452.

(42) Jain, P. K.; Lee, K. S.; El-Sayed, I. H.; El-sayed, M. A. Calculated Absorption and Scattering Properties of Gold Nanoparticles of Different Size, Shape, and Composition: Applications in Biological Imaging and Biomedicine. *J. Phys. Chem. B* **2006**, *110*, 7238−7248.

(43) Van Dijk, M. A.; Tchebotareva, A. L.; Orrit, M.; Lippitz, M.; Berciaud, S.; Lasne, D.; Cognet, L.; Lounis, B. Absorption and Scattering Microscopy of Single Metal Nanoparticles. *Phys. Chem. Chem. Phys.* **2006**, *8*, 3486−3495.

(44) Kale, M. J.; Avanesian, T.; Christopher, P. Direct Photocatalysis by Plasmonic Nanostructures. *ACS Catal.* 2014, 4, 116−128.

(45) Boerigter, C.; Campana, R.; Morabito, M.; Linic, S. Evidence and Implications of Direct Charge Excitation as the Dominant Mechanism in Plasmon-Mediated Photocatalysis. *Nat. Commun.* 2016, 7, 10545.

(46) Ashcroft, N. W.; Mermin, N. D. *Solid State Physics*; Saunders College: Philadelphia, 1976; pp 9−49.

(47) Doremus, R. H. Optical Properties of Small Gold Particles. *J. Chem. Phys.* 1964, 40, 2389−2396.

(48) Besteiro, L. V.; Govorov, A. O. Amplified Generation of Hot Electrons and Quantum Surface Effects in Nanoparticle Dimers with Plasmonic Hot Spots. *J. Phys. Chem. C* 2016, 120, 19329−19339.

(49) Brown, A. M.; Sundararaman, R.; Narang, P.; Schwartzberg, A. M.; Goddard, W. A.; Atwater, H. A. Experimental and *Ab Initio* Ultrafast Carrier Dynamics in Plasmonic Nanoparticles. *Phys. Rev. Lett.* 2017, 118, 087401.

(50) Deeb, C.; Zhou, X.; Plain, J.; Wiederrecht, G. P.; Bachelot, R.; Russell, M.; Jain, P. K. Size Dependence of the Plasmonic Near-Field Measured *via* Single-Nanoparticle Photoimaging. *J. Phys. Chem. C* 2013, 117, 10669−10676.

(51) Amendola, V.; Meneghetti, M. Exploring How to Increase the Brightness of Surface-Enhanced Raman Spectroscopy Nanolabels: The Effect of the Raman-Active Molecules and of the Label Size. *Adv. Funct. Mater.* 2012, 22, 353−360.

(52) Starowicz, Z.; Wojnarowska-Nowak, R.; Ozga, P.; Sheregii, E. M. The Tuning of the Plasmon Resonance of the Metal Nanoparticles in Terms of the SERS Effect. *Colloid Polym. Sci.* 2018, 296, 1029−1037.

(53) Long, R.; Li, Y.; Song, L.; Xiong, Y. Coupling Solar Energy into Reactions: Materials Design for Surface Plasmon-Mediated Catalysis. *Small* 2015, 11, 3873−3889.

(54) Zhang, Z.; Gernert, U.; Gerhardt, R. F.; Höhn, E. M.; Belder, D.; Kneipp, J. Catalysis by Metal Nanoparticles in a Plug-In Optofluidic Platform: Redox Reactions of *p*-Nitrobenzenethiol and *p*-Aminothiophenol. *ACS Catal.* 2018, 8, 2443−2449.

(55) Marinica, D.-C.; Aizpurua, J.; Borisov, A. G. Quantum Effects in the Plasmon Response of Bimetallic Core-Shell Nanostructures. *Opt. Express* 2016, 24, 23941.

(56) Griffin, S.; Montoni, N. P.; Li, G.; Straney, P. J.; Millstone, J. E.; Masiello, D. J.; Camden, J. P. Imaging Energy Transfer in Pt-Decorated Au Nanoprisms *via* Electron Energy-Loss Spectroscopy. *J. Phys. Chem. Lett.* 2016, 7, 3825−3832.

(57) Li, J. F.; Yang, Z. L.; Ren, B.; Liu, G. K.; Fang, P. P.; Jiang, Y. X.; Wu, D. Y.; Tian, Z. Q. Surface-Enhanced Raman Spectroscopy Using Gold-Core Platinum-Shell Nanoparticle Film Electrodes: Toward a Versatile Vibrational Strategy for Electrochemical Interfaces. *Langmuir* 2006, 22, 10372−10379.

(58) Murray, C. A. Using Surface Enhanced Raman Scattering to Study Vibrations of Adsorbates on Thin Metallic Overlayers on Silver. *J. Electron Spectrosc. Relat. Phenom.* 1983, 29, 371−382.

(59) Zou, S.; Weaver, M. J. Surface-Enhanced Raman Scattering on Uniform Transition-Metal Films: Toward a Versatile Adsorbate Vibrational Strategy for Solid-Nonvacuum Interfaces? *Anal. Chem.* 1998, 70, 2387−2395.

(60) Zhang, K.; Xiang, Y.; Wu, X.; Feng, L.; He, W.; Liu, J.; Zhou, W.; Xie, S. Enhanced Optical Responses of Au@Pd Core/Shell Nanobars. *Langmuir* 2009, 25, 1162−1168.

(61) Patterson, J. LXXII. On the Electrical Properties of Thin Metal Films. *London, Edinburgh, Dublin Philos. Mag. J. Sci.* 1902, 4, 652−678.

(62) Fischer, G.; Hoffmann, H.; Vancea, J. Mean Free Path and Density of Conductance Electrons in Platinum Determined by the Size Effect in Extremely Thin Films. *Phys. Rev. B: Condens. Matter Mater. Phys.* 1980, 22, 6065−6073.

(63) Dutta, S.; Sankaran, K.; Moors, K.; Pourtois, G.; Van Elshocht, S.; Bömmels, J.; Vandervorst, W.; Tokei, Z.; Adelmann, C. Thickness Dependence of the Resistivity of Platinum-Group Metal Thin Films. *J. Appl. Phys.* 2017, 122, 025107.

(64) Gall, D. The Search for the Most Conductive Metal for Narrow Interconnect Lines. *J. Appl. Phys.* 2020, 127, 050901.

(65) Voisin, C.; Del Fatti, N.; Christofilos, D.; Vallée, F. Ultrafast Electron Dynamics and Optical Nonlinearities in Metal Nanoparticles. *J. Phys. Chem. B* 2001, 105, 2264−2280.

(66) Heilweil, E. J.; Hochstrasser, R. M. Nonlinear Spectroscopy and Picosecond Transient Grating Study of Colloidal Gold. *J. Chem. Phys.* 1985, 82, 4762−4770.

(67) Ahmadi, T. S.; Logunov, S. L.; El-Sayed, M. A. Picosecond Dynamics of Colloidal Gold Nanoparticles. *J. Phys. Chem.* 1996, 100, 8053−8056.

(68) Perner, M.; Bost, P.; Lemmer, U.; Von Plessen, G.; Feldmann, J.; Becker, U.; Mennig, M.; Schmitt, M.; Schmidt, H. Optically Induced Damping of the Surface Plasmon Resonance in Gold Colloids. *Phys. Rev. Lett.* 1997, 78, 2192−2195.

(69) Hodak, J. H.; Martini, I.; Hartland, G. V. Spectroscopy and Dynamics of Nanometer-Sized Noble Metal Particles. *J. Phys. Chem. B* 1998, 102, 6958−6967.

(70) Smith, B. A.; Waters, D. M.; Faulhaber, A. E.; Kreger, M. A.; Roberti, T. W.; Zhang, J. Z. Preparation and Ultrafast Optical Characterization of Metal and Semiconductor Colloidal Nano-Particles. *J. Sol-Gel Sci. Technol.* 1997, 9, 125−137.

(71) Faulhaber, A. E.; Smith, B. A.; Andersen, J. K.; Zhang, J. Z. Femtosecond Electronic Relaxation Dynamics in Metal Nano-Particles: Effects of Surface and Size Confinement. *Mol. Cryst. Liq. Cryst. Sci. Technol., Sect. A* 1996, 283, 25−30.

(72) Link, S.; Burda, C.; Wang, Z. L.; El-Sayed, M. A. Electron Dynamics in Gold and Gold-Silver Alloy Nanoparticles: The Influence of a Nonequilibrium Electron Distribution and the Size Dependence of the Electron-Phonon Relaxation. *J. Chem. Phys.* 1999, 111, 1255−1264.

(73) Hodak, J. H.; Henglein, A.; Hartland, G. V. Tuning the Spectral and Temporal Response in PtAu Core-Shell Nanoparticles. *J. Chem. Phys.* 2001, 114, 2760−2765.

(74) Hodak, J. H.; Henglein, A.; Hartland, G. V. Photophysics of Nanometer Sized Metal Particles: Electron−Phonon Coupling and Coherent Excitation of Breathing Vibrational Modes. *J. Phys. Chem. B* 2000, 104, 9954−9965.

(75) Broyer, M.; Cottancin, E.; Lermé, J.; Pellarin, M.; Del Fatti, N.; Vallée, F.; Burgin, J.; Guillon, C.; Langot, P. Optical Properties and Relaxation Processes at Femtosecond Scale of Bimetallic Clusters. *Faraday Discuss.* 2008, 138, 137−145.

(76) Zarick, H. F.; Boulesbaa, A.; Talbert, E. M.; Puretzky, A.; Geohegan, D.; Bardhan, R. Ultrafast Excited-State Dynamics in Shape- and Composition-Controlled Gold-Silver Bimetallic Nano-structures. *J. Phys. Chem. C* 2017, 121, 4540−4547.

(77) Yu, K.; You, G.; Polavarapu, L.; Xu, Q. H. Bimetallic Au/Ag Core-Shell Nanorods Studied by Ultrafast Transient Absorption Spectroscopy under Selective Excitation. *J. Phys. Chem. C* 2011, 115, 14000−14005.

(78) Hodak, J. H.; Henglein, A.; Hartland, G. V. Coherent Excitation of Acoustic Breathing Modes in Bimetallic Core-Shell Nanoparticles. *J. Phys. Chem. B* 2000, 104, 5053−5055.

(79) Kirakosyan, A. S.; Shahbazyan, T. V. Vibrational Modes of Metal Nanoshells and Bimetallic Core-Shell Nanoparticles. *J. Chem. Phys.* 2008, 129, 034708.

(80) Yu, S.; Zhang, J.; Tang, Y.; Ouyang, M. Engineering Acoustic Phonons and Electron-Phonon Coupling by the Nanoscale Interface. *Nano Lett.* 2015, 15, 6282−6288.

(81) Stoll, T.; Maioli, P.; Crut, A.; Burgin, J.; Langot, P.; Pellarin, M.; Sánchez-Iglesias, A.; Rodríguez-González, B.; Liz-Marzán, L. M.; Del Fatti, N.; Vallée, F. Ultrafast Acoustic Vibrations of Bimetallic Nanoparticles. *J. Phys. Chem. C* 2015, 119, 1591−1599.

(82) Seah, M. P. Simple Universal Curve for the Energy-Dependent Electron Attenuation Length for All Materials. *Surf. Interface Anal.* 2012, 44, 1353−1359.

(83) Citrin, P. H.; Wertheim, G. K.; Baer, Y. Core-Level Binding Energy and Density of States from the Surface Atoms of Gold. *Phys. Rev. Lett.* 1978, 41, 1425−1428.

(84) Miller, D. J.; Øberg, H.; Kaya, S.; Sanchez Casalongue, H.; Friebel, D.; Anniyev, T.; Ogasawara, H.; Bluhm, H.; Pettersson, L. G. M.; Nilsson, A. Oxidation of Pt(111) under Near-Ambient Conditions. *Phys. Rev. Lett.* **2011**, *107*, 195502.

(85) Stadnichenko, A. I.; Murav'ev, V. V.; Svetlichnyi, V. A.; Boronin, A. I. Platinum State in Highly Active Pt/CeO2 Catalysts from the X-Ray Photoelectron Spectroscopy Data. *J. Struct. Chem.* **2017**, *58*, 1152−1159.

(86) Axnanda, S.; Crumlin, E. J.; Mao, B.; Rani, S.; Chang, R.; Karlsson, P. G.; Edwards, M. O. M.; Lundqvist, M.; Moberg, R.; Ross, P.; Hussain, Z.; Liu, Z. Using "Tender" X-Ray Ambient Pressure X-Ray Photoelectron Spectroscopy as A Direct Probe of Solid-Liquid Interface. *Sci. Rep.* **2015**, *5*, 9788.

(87) Park, J. Y.; Aliaga, C.; Renzas, J. R.; Lee, H.; Somorjai, G. A. The Role of Organic Capping Layers of Platinum Nanoparticles in Catalytic Activity of CO Oxidation. *Catal. Lett.* **2009**, *129*, 1−6.

(88) Prieto, M. J.; Carbonio, E. A.; Fatayer, S.; Landers, R.; Siervo, A. d. Electronic and Structural Study of Pt-Modified Au Vicinal Surfaces: A Model System for Pt-Au Catalysts. *Phys. Chem. Chem. Phys.* **2014**, *16*, 13329−13339.

(89) Prieto, M. J.; Carbonio, E. A.; Landers, R.; De Siervo, A. Promotion Effect of Platinum on Golds Reactivity: A High-Resolution Photoelectron Spectroscopy Study. *J. Phys. Chem. C* **2016**, *120*, 10227−10236.

(90) Tereshchuk, P.; Freire, R. L. H.; Da Silva, J. L. F. The Role of the CO Adsorption on Pt Monolayers Supported on Flat and Stepped Au Surfaces: A Density Functional Investigation. *RSC Adv.* **2014**, *4*, 9247−9254.

(91) Pedersen, M. Ø.; Helveg, S.; Ruban, A.; Stensgaard, I.; Lægsgaard, E.; Nørskov, J. K.; Besenbacher, F. How a Gold Substrate Can. Increase the Reactivity of a Pt Overlayer. *Surf. Sci.* **1999**, *426*, 395−409.

(92) Freire, R. L. H.; Kiejna, A.; Da Silva, J. L. F. Adsorption of Rh, Pd, Ir, and Pt on the Au(111) and Cu(111) Surfaces: A Density Functional Theory Investigation. *J. Phys. Chem. C* **2014**, *118*, 19051−19061.

(93) Chatzidakis, M.; Prabhudev, S.; Saidi, P.; Chiang, C. N.; Hoyt, J. J.; Botton, G. A. Bulk Immiscibility at the Edge of the Nanoscale. *ACS Nano* **2017**, *11*, 10984−10991.

(94) Braidy, N.; Purdy, G. R.; Botton, G. a. Equilibrium and Stability of Phase-Separating Au−Pt Nanoparticles. *Acta Mater.* **2008**, *56*, 5972−5983.

(95) Reyes-Nava, J. A.; Rodríguez-López, J. L.; Pal, U. Generalizing Segregation and Chemical Ordering in Bimetallic Nanoclusters through Atomistic View Points. *Phys. Rev. B: Condens. Matter Mater. Phys.* **2009**, *80*, 161412.

(96) Deng, L.; Hu, W.; Deng, H.; Xiao, S. Surface Segregation and Structural Features of Bimetallic Au− Pt Nanoparticles. *J. Phys. Chem. C* **2010**, *114*, 11026−11032.

(97) Lin, Z.; Zhigilei, L. V.; Celli, V. Electron-Phonon Coupling and Electron Heat Capacity of Metals under Conditions of Strong Electron-Phonon Nonequilibrium. *Phys. Rev. B: Condens. Matter Mater. Phys.* **2008**, *77*, 075133.

(98) Etchegoin, P. G.; Le Ru, E. C.; Meyer, M. An Analytic Model for the Optical Properties of Gold. *J. Chem. Phys.* **2006**, *125*, 164705.

(99) Johnson, P. B.; Christy, R. W. Optical Constants of the Noble Metals. *Phys. Rev. B* **1972**, *6*, 4370−4379.

(100) Rioux, D.; Vallières, S.; Besner, S.; Muñoz, P.; Mazur, E.; Meunier, M. An Analytic Model for the Dielectric Function of Au, Ag, and Their Alloys. *Adv. Opt. Mater.* **2014**, *2*, 176−182.

(101) Derkachova, A.; Kolwas, K.; Demchenko, I. Dielectric Function for Gold in Plasmonics Applications: Size Dependence of Plasmon Resonance Frequencies and Damping Rates for Nanospheres. *Plasmonics* **2016**, *11*, 941−951.

(102) Myroshnychenko, V.; Rodríguez-Fernández, J.; Pastoriza-Santos, I.; Funston, A. M.; Novo, C.; Mulvaney, P.; Liz-Marzán, L. M.; García de Abajo, F. J. Modelling the Optical Response of Gold Nanoparticles. *Chem. Soc. Rev.* **2008**, *37*, 1792−1805.

(103) Roaf, D. J. The Fermi Surfaces of Copper, Silver and Gold II. Calculation of the Fermi Surfaces. *Philos. Trans. R. Soc. A Math. Phys. Eng. Sci.* **1962**, *255*, 135−152.

(104) Beversluis, M.; Bouhelier, A.; Novotny, L. Continuum Generation from Single Gold Nanostructures through Near-Field Mediated Intraband Transitions. *Phys. Rev. B: Condens. Matter Mater. Phys.* **2003**, *68*, 155433.

(105) Glantschnig, K.; Ambrosch-Draxl, C. Relativistic Effects on the Linear Optical Properties of Au, Pt, Pb and W. *New J. Phys.* **2010**, *12*, 103048.

(106) Henglein, A. Preparation and Optical Aborption Spectra of $Au_{core}Pt_{shell}$ and PtcoreAushell Colloidal Nanoparticles in Aqueous Solution. *J. Phys. Chem. B* **2000**, *104*, 2201−2203.

(107) Creighton, J. A.; Eadon, D. G. Ultraviolet-Visible Absorption Spectra of the Colloidal Metallic Elements. *J. Chem. Soc., Faraday Trans.* **1991**, *87*, 3881−3891.

(108) Davis-Wheeler Chin, C.; Akbarian-Tefaghi, S.; Reconco-Ramirez, J.; Wiley, J. B. Rapid Microwave Synthesis and Optical Activity of Highly Crystalline Platinum Nanocubes. *MRS Commun.* **2018**, *8*, 71−78.

(109) Cholach, A. R.; Tapilin, V. M. Electronic Structure of the Pt(100) Single Crystal Surface Affected by Oxygen Adsorption. *React. Kinet. Catal. Lett.* **2005**, *86*, 315−321.

(110) Teperik, T. V.; Nordlander, P.; Aizpurua, J.; Borisov, A. G. Quantum Effects and Nonlocality in Strongly Coupled Plasmonic Nanowire Dimers. *Opt. Express* **2013**, *21*, 27306.

(111) Liebsch, A. Surface-Plasmon Dispersion and Size Dependence of Mie Resonance: Silver *versus* Simple Metals. *Phys. Rev. B: Condens. Matter Mater. Phys.* **1993**, *48*, 11317−11328.

(112) Sönnichsen, C.; Franzl, T.; Wilk, T.; von Plessen, G.; Feldmann, J.; Wilson, O.; Mulvaney, P. Drastic Reduction of Plasmon Damping in Gold Nanorods. *Phys. Rev. Lett.* **2002**, *88*, 077402.

(113) Zadoyan, R.; Seferyan, H. Y.; Wark, A. W.; Corn, R. M.; Apkarian, V. A. Interfacial Velocity-Dependent Plasmon Damping in Colloidal Metallic Nanoparticles. *J. Phys. Chem. C* **2007**, *111*, 10836−10840.

(114) Kreibig, U.; Vollmer, M. *Optical Properties of Metal Clusters*; Springer Series in Materials Science; Springer: Berlin, Heidelberg, 1995; Vol. 25.

(115) Zhang, H.; Govorov, A. O. Optical Generation of Hot Plasmonic Carriers in Metal Nanocrystals: The Effects of Shape and Field Enhancement. *J. Phys. Chem. C* **2014**, *118*, 7606−7614.

(116) Kirakosyan, A. S.; Stockman, M. I.; Shahbazyan, T. V. Surface Plasmon Lifetime in Metal Nanoshells. *Phys. Rev. B: Condens. Matter Mater. Phys.* **2016**, *94*, 155429.

(117) Hu, M.; Hartland, G. V. Heat Dissipation for Au Particles in Aqueous Solution: Relaxation Time *versus* Size. *J. Phys. Chem. B* **2002**, *106*, 7029−7033.

(118) Pudell, J.; Maznev, A. A.; Herzog, M.; Kronseder, M.; Back, C. H.; Malinowski, G.; von Reppert, A.; Bargheer, M. Layer Specific Observation of Slow Thermal Equilibration in Ultrathin Metallic Nanostructures by Femtosecond X-Ray Diffraction. *Nat. Commun.* **2018**, *9*, 3335.

(119) Wang, W.; Cahill, D. G. Limits to Thermal Transport in Nanoscale Metal Bilayers Due to Weak Electron-Phonon Coupling in Au and Cu. *Phys. Rev. Lett.* **2012**, *109*, 175503.

(120) Touloukian, Y. S.; Powell, R. W.; Ho, C. Y.; Klemens, P. G. *Thermophysical Properties of Matter - the TPRC Data Series. Vol. 1. Thermal Conductivity - Metallic Elements and Alloys. (Reannouncement). Data Book*; IFI/Plenum Data Coorporation: New York, 1970; pp 132−137, 262−269.

(121) Wang, H.-D.; Liu, J.-H.; Zhang, X.; Guo, Z.-Y.; Takahashi, K. Experimental Study on the Influences of Grain Boundary Scattering on the Charge and Heat Transport in Gold and Platinum Nanofilms. *Heat Mass Transfer* **2011**, *47*, 893−898.

(122) Fann, W. S.; Storz, R.; Tom, H. W. K.; Bokor, J. Electron Thermalization in Gold. *Phys. Rev. B: Condens. Matter Mater. Phys.* **1992**, *46*, 13592−13595.

(123) Hartland, G. V. Coherent Excitation of Vibrational Modes in Metallic Nanoparticles. *Annu. Rev. Phys. Chem.* **2006**, *57*, 403−430.

(124) Belotskii, E. D.; Tomchuk, P. M. Surface Electron-Phonon Energy Exchange in Small Metallic Particles. *Int. J. Electron.* **1992**, *73*, 955−957.

(125) Belotskii, E. D.; Tomchuk, P. M. Electron-Phonon Interaction and Hot Electrons in Small Metal Islands. *Surf. Sci.* **1990**, *239*, 143−155.

(126) Schneider, C. A.; Rasband, W. S.; Eliceiri, K. W. NIH Image to ImageJ: 25 Years of Image Analysis. *Nat. Methods* **2012**, *9*, 671−675.

(127) Hörnström, S. E.; Johansson, L.; Flodström, A.; Nyholm, R.; Schmidt-May, J. Surface and Bulk Core Level Binding Energy Shifts in Pt-Au Alloys. *Surf. Sci.* **1985**, *160*, 561−570.

(128) Wertheim, G. K.; Citrin, P. H. *Photoemission in Solids I*; Cardona, M., Ley, L., Eds.; Topics in Applied Physics; Springer: Berlin, Heidelberg, 1978; Vol. *26*.